THE ν_1 VIBRATIONAL RAMAN SPECTRA OF SOLID METHANE

PING XIAO

INFORMATION TO USERS

This manuscript has been reproduced from the microfilm master. UMI films the text directly from the original or copy submitted. Thus, some thesis and dissertation copies are in typewriter face, while others may be from any type of computer printer.

The quality of this reproduction is dependent upon the quality of the copy submitted. Broken or indistinct print, colored or poor quality illustrations and photographs, print bleedthrough, substandard margins, and improper alignment can adversely affect reproduction.

In the unlikely event that the author did not send UMI a complete manuscript and there are missing pages, these will be noted. Also, if unauthorized copyright material had to be removed, a note will indicate the deletion.

Oversize materials (e.g., maps, drawings, charts) are reproduced by sectioning the original, beginning at the upper left-hand corner and continuing from left to right in equal sections with small overlaps. Each original is also photographed in one exposure and is included in reduced form at the back of the book.

Photographs included in the original manuscript have been reproduced xerographically in this copy. Higher quality 6" x 9" black and white photographic prints are available for any photographs or illustrations appearing in this copy for an additional charge. Contact UMI directly to order.

UMI

A Bell & Howell Information Company
300 North Zeeb Road, Ann Arbor MI 48106-1346 USA
313/761-4700 800/521-0600

THE ν_1 VIBRATIONAL RAMAN SPECTRA OF SOLID METHANE

Ping XIAO

A THESIS SUBMITTED IN PARTIAL
FULFILLMENT OF THE REQUIREMENTS
FOR
THE DEGREE OF
MASTER OF SCIENCE

DEPARTMENT OF PHYSICS
MEMORIAL UNIVERSITY OF NEWFOUNDLAND

Abstract

The ν_1 vibrational Raman spectra of oriented CH_4 single crystals have been measured in the temperature range from 89.4 K to 21.8 K. The experimental results show that the frequency, width and the depolarization ratio of the spectra change with the temperature and the orientation of the crystals. We think these changes are connected to the following factors: (1) Volume changes; (2) Vibration-rotation (coriolis type) interactions; (3) Probably molecular orientation change in some temperature range.

Acknowledgements

It is a great pleasure to express my sincere appreciation to my supervisors, Dr. M. J. Clouter and Dr. H. Kiefte, for their constant support and guidance throughout this project. I would like to thank Dr. J. C. Lewis, Dr. C. W. Cho and Dr. N. H. Rich for their helpful discussions with me. I am grateful to Dr. R. Goulding for his help in solving experimental problems. I am also thankful to Mr. O. Vazquez for his computer program of the data acquisition and control system.

Contents

List of Figures

List of Tables

Chapter 1

Introduction

1.1 Introduction

The methane systems have been of interest both experimentally and theoretically for many years because they exhibit some imporant characteristics of a simple system, for example, having tight internal bonding, weak external coupling between molecules, and a highly symmetric molecular structure (T_d for CH_4 and CD_4) [1].

Methane may also be important in the structure of the outer planets, and gaseous methane exists in the atmospheres of most of them. Liquid or solid methane may be a major constituent of the "icy giants" such as Uranus and Neptune.

Many people did research for the methane systems. Clusius [3] discovered the anomaly of the specific heat of solid methane at 20.4 K in 1929. Trapeznikowa and Miljution [4] found that at a pressure of 1 kg/cm^2 the anomaly of specific heat occurred at 20.6 K.

X-ray studies on crystalline CH_4 by Schallamach [30] indicated that the molecular lattice (carbon lattice) is face-centered cubic both above and below 20.4 K.

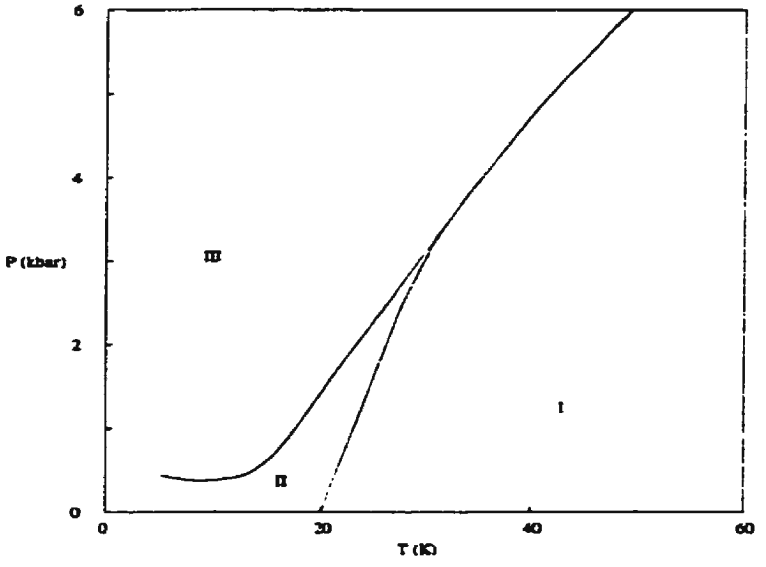

Figure 1.1: Schematic Phase Diagram of Solid CH_4

Figure 1.1 shows schematically the phase diagram of solid CH_4 [6, 7]. At low pressures, there are two phases for CH_4, phase I and phase II. The phase III can only occur at pressure above 200 *atm* [8]. The phase I has a fcc structure with disordered molecules. The structure of phase II was predicted by James and Keenan [9] on the basis of a classical mean field theory, assuming electrostatic octupole-octupole interactions between molecules located on a fcc lattice. This structure consists of eight sublattices (Section 2.3). The molecules on six of these sublattices (D_{2d}) are ordered in such a way that

their octupole interactions with molecules on the other two sublattices add to zero and, thus, the molecules on these two sublatices (O) rotate freely. In 1972 Press [26] established by neutron scattering that the phase II of CD_4 and by inference also the phase II of CH_4 did in fact correspond to the James and Keenan structure. For phase I of CD_4, Press detected an indication of partial order at 77 K, and this indication disappeared at 35 K. He concluded that the molecular orientations are completely disordered at 35 K.

Medina [10] did far-infrared studies of solid CH_4 and found five infrared active lattice modes at range from 49.6 cm^{-1} to 105.3 cm^{-1} for phase III. The lowest frequency mode was identified as librational mode while all others were identified as translational modes.

The vibrational Raman spectrum is an important method to study molecular vibrations and symmetries. The molecular vibrations in solids, liquids and gases manifest themselves in light scattering as distinct lines or bands displaced by some frequency shifts from the exciting line of the incident radiation. The measurement of the vibrational Raman spectra could give us directly the vibrational frequencies of the molecules. Apart from its frequency shift, the structure, intensity, and polarization of the Raman spectra also give us an insight into the geometry of the particular mode of vibration which gives rise to it [44].

Anderson and Savoie [29] measured the Raman spectra of crystalline CH_4 and CD_4 at 10 K and 77 K in 1965. They observed ν_1, ν_2 and ν_3. They found marked changes in the spectra at the transition phase I - phase II. For ν_1 of

CH_4, the fairly sharp, single band in phase I (FWHM $\simeq$ 4 cm^{-1}) splitted into a doublet in phase II; For ν_3, the very broad band (FWHM $\simeq$ 100 cm^{-1}) of the high-temperature phase was transformed into a much sharper peak (FWHM $\simeq$ 3 cm^{-1}) at lower frequency, together with a weaker and broader band at high frequencies; For ν_2 of CH_4, the singlet in phase I splitted into a doublet in phase II.

In recent years, lasers have become invaluable tools for the study of Raman spectra. The main advantages of the laser source are the following:

(1) The radiation from a laser source is generally monochromatic, the width of the laser line can be very small ($\leq$ 0.005 cm^{-1}), and therefore the Raman spectra are easier to analyze and precise information can be obtained on the width and fine structure of the Raman line.

(2) The very small sectional area, negligible divergence, and high specific intensity of the laser radiation permit the use of small quantities of the substances. The source could be kept far away from the sample, thus eliminating the heating effect and other disturbing factors.

(3) The linear polarization and the perfect geometry between the direction of illumination and observation which one has by the use of the laser enable one to make accurate measurements of the depolarization ratio of the Raman lines.

Using the laser, Cabana and Thé [27] measured the Raman spectra of

solid CH_4 in phase II. They got ν_1, ν_2, ν_3 and two weak bands in the lattice vibration region. For ν_1, they observed two peaks, the lower intensity one at the higher frequency side (2908.6 cm^{-1}) was attributable to rotating molecules, and the higher intensity one (2903.1 cm^{-1}) to D_{2d} molecules. For ν_2, they got a doublet corresponding to the O molecules and D_{2d} molecules. In the ν_3 band, they identified several rotational components due to the rotating molecules. The spectrum was consistent with the structure originally proposed by James and Keenan [9]. Their experimental results were in good agreement with the theoretical values based on the extended James-Keenan model by Yamamoto and coworkers [11].

Clouter, Kiefte and Jain [14] measured ν_1 Raman spectra of liquid CH_4 and observed the density dependence of frequency and the temperature dependence of width.

Rose, Whitewolf, and Baglin [42] measured the Raman spectra for ν_1 mode of high density gaseous CH_4 in 1992. They found the nonzero depolarization ratio and measured its pressure (density) dependence.

Fabre, Thiéry, Vu and Kobashi [6, 12, 28] measured the Raman spectra of solid CH_4 at 4.2 K under high pressure in 1978, 1982 and 1985 (0.1 to 11 kbar). They obtained six phases at different pressures.

Sharma, Mao, and Bell [13] did Raman experiments for solid CH_4 at high pressure (16 to 187 kbar) at room temperature in 1979. They found that phase VI has more than two molecules in the unit cell (at least three $\nu_1(A_1)$

bands).

Culler and Schiferl [2] did the Raman experiment at high temperature and high pressure in 1993 (up to 13 GPa, 912 K). They found that at 2.5 - 5.0 GPa and 912 K, methane photoreacts with the laser light and forms a graphitelike soot compound.

In this work, we study the ν_1 vibrational Raman spectra of oriented CH_4 single crystals.

Chapter 2

Molecular Vibrations

2.1 Molecular Vibrations

For a molecule of N atoms, the kinetic energy is given by[15, 16]

$$T = \frac{1}{2}\sum_{\alpha=1}^{N} m_\alpha[(\frac{d\Delta x_\alpha}{dt})^2 + (\frac{d\Delta y_\alpha}{dt})^2) + (\frac{d\Delta z_\alpha}{dt})^2], \tag{2.1}$$

where $x_\alpha, y_\alpha, z_\alpha$ are the cartesian coordinates of αth atom with mass m_α, Δx_α, Δy_α, and Δz_α are the displacements from the equilibrium position.

In terms of the mass-weighted cartesian displacement coordinates, $q_1, q_2, ..., q_{3N}$,

$$q_1 = \sqrt{m_1}\Delta x_1, q_2 = \sqrt{m_1}\Delta y_1, q_3 = \sqrt{m_1}\Delta z_1, q_4 = \sqrt{m_2}\Delta x_2, ..., q_{3N} = \sqrt{m_N}\Delta z_N, \tag{2.2}$$

$$T = \frac{1}{2}\sum_{i=1}^{3N} \dot{q}_i^2. \tag{2.3}$$

For small displacements, the potential energy V may be expressed as

$$V = V_0 + \sum_{i=1}^{3N} f_i q_i + \frac{1}{2}\sum_{i=1}^{3N} f_{ij} q_i q_j + \textit{higher terms}, \tag{2.4}$$

where $f_i = (\frac{\partial V}{\partial q_i})_0$, and $f_{ij} = (\frac{\partial^2 V}{\partial q_i \partial q_j})_0$.

By choosing the zero of energy so that the energy of the equilibrium configuration is zero, $V_0 = 0$. Furthermore, when all atoms are in their equilibrium positions, $q_i = 0, i = 1, 2, ..., 3N$, the energy must be a minimum, therefore

$$f_i = (\frac{\partial V}{\partial q_i})_0 = 0, \quad i = 1, 2, ..., 3N.$$

For sufficiently small amplitudes of vibration, the higher terms can be neglected, so that

$$V = \frac{1}{2}\sum_{i=1}^{3N} f_{ij} q_i q_j. \tag{2.5}$$

We can introduce normal coordinates by linear transformation,

$$Q_k = \sum_{i=1}^{3N} c_{ki} q_i, \quad k = 1, 2, ..., 3N \tag{2.6}$$

in which the coefficients c_{ki} have been chosen so that both T and V have simpler forms,

$$T = \frac{1}{2}\sum_{k=1}^{3N} \dot{Q}_k^2, \tag{2.7}$$

$$V = \frac{1}{2}\sum_{k=1}^{3N} \lambda_k Q_k^2. \tag{2.8}$$

The λ_k can be shown to be the roots of the secular equation:

$$\begin{vmatrix} f_{11} - \lambda & f_{12} & \cdots & f_{1,3N} \\ f_{21} & f_{22} - \lambda & \cdots & f_{2,3N} \\ \cdots & \cdots & \cdots & \cdots \\ f_{3N,1} & f_{3N,2} & \cdots & f_{3N,3N} - \lambda \end{vmatrix} = 0 \tag{2.9}$$

Using Lagrangian methods, the equations of motion become

$$\frac{d}{dt}\frac{\partial T}{\partial \dot{Q}_k} + \frac{\partial V}{\partial Q_k} = \bar{Q}_k + \lambda_k Q_k = 0 \qquad (2.10)$$

$$k = 1, 2, ..., 3N$$

The solutions of which are

$$Q_k = K_k' cos(2\pi\nu_k t + \varphi_k) \qquad (2.11)$$

$$k = 1, 2, .., 3N$$

where $\nu_k = \frac{1}{2\pi}\lambda_k^{\frac{1}{2}}$.

The solutions for q_i are

$$q_i = \sum_{k=1}^{3N}(c^{-1})_{ik}K_k' cos(2\pi\nu_k t + \varphi_k) = \sum_{k=1}^{3N} c_{ki}K_k' cos(2\pi\nu_k t + \varphi_k). \qquad (2.12)$$

The secular equation 2.9 has five or six roots that are equal to zero [16], depending on whether the system is linear or not. They correspond to translations and rotations. It can be shown that all other 3N-5 or 3N-6 roots are different from zero and real. Thus we have 3N-5 or 3N-6 genuine normal vibrations.

In quantum mechanics, the Schrödinger equation of the system is

$$\sum_\alpha \frac{1}{m_\alpha}\left(\frac{\partial^2\psi_v}{\partial x_i^2} + \frac{\partial^2\psi_v}{\partial y_i^2} + \frac{\partial^2\psi_v}{\partial z_i^2}\right) + \frac{8\pi^2}{h^2}(E - V)\psi_v = 0 \qquad (2.13)$$

where ψ_v is the vibrational wave function, E is the total vibrational energy, and V is the potential energy. In terms of the normal coordinates Q_k, the Schrödinger equation will have the form [15]

$$\sum_{k=1}^{3N-6}\frac{\partial^2\psi_v}{\partial Q_k^2} + \frac{8\pi^2}{h^2}\left(E - \frac{1}{2}\sum_{k=1}^{3N-6}\lambda_k Q_k^2\right)\psi_v = 0. \qquad (2.14)$$

Equation 2.14 can be separated into $3N-6$ equations:

$$\frac{1}{\psi_k}\frac{\partial^2\psi_k}{\partial Q_k^2}+\frac{8\pi^2}{h^2}(E-\frac{1}{2}\lambda_k Q_k^2)=0, \tag{2.15}$$

where

$$\psi_v=\psi_1(Q_1)\psi_2(Q_2)...\psi_{3N-6}(Q_{3N-6}) \tag{2.16}$$

$$E=E_1+E_2+...+E_{3N-6}. \tag{2.17}$$

The equation 2.15 is the wave equation of a simple harmonic oscillator of potential energy $\frac{1}{2}\lambda_k Q_k^2$ and mass 1 whose coordinate is the normal coordinate Q_k. The eigenfunction is given by

$$\psi_k(Q_k)=N_{v_k}e^{-\frac{1}{2}\gamma_k Q_k^2}H_{v_k}(\sqrt{\gamma_k}Q_k) \tag{2.18}$$

Here N_{V_k} is the normalizing factor, $\gamma_k=4\pi^2\nu_k/h$, and $H_{V_k}(\sqrt{\gamma_k}Q_k)$ is a Hermite polynomial (of degree v_k in Q_k).

Thus the vibrational motion of the molecule may be considered as a superposition of $3N-6$ simple harmonic motions in the $3N-6$ normal coordinates. The total vibrational eigenfunction ψ_v is the product of $3N-6$ harmonic oscillastor functions $\psi_k(Q_k)$. The total vibrational energy E is the sum of the energies of $3N-6$ harmonic oscillators, given by

$$E=\sum_{k=1}^{3N-6}h\nu_k(v_k+\frac{1}{2}). \tag{2.19}$$

2.2 Molecular Vibrations in CH_4

The CH_4 molecule belongs to T_d point group [16]. The four H atoms in CH_4 form a regular tetrahedron whose centre is occupied by the C atom.

Figure 2.1 shows the tetrahedron structure [16, 17]. There are three mutually perpendicular C_2 axes, three S_4 axes coinciding with C_2 axes, four C_3 axes each of which passes through one apex and the center of the opposite face, and six planes of symmetry σ_d – each of the planes passes through one pair of C_3 axes. The total number of symmetry operations is 24 ($E + 8C_3 + 3C_2 + 6S_4 + 6\sigma_d$).

Table 2.1 gives the symmetry types and the characters for the point group T_d [16]. In the last column is given the non-genuine vibrations, translations (T_x, T_y, T_z), and rotations (R_x, R_y, R_z) that belong to the particular species.

There are two types (A_1 and A_2) of non-degenerate vibrations or eigenfunctions. A_1 is a totally symmetric type. The vibration or eigenfunction of A_2 is symmetric with respect to C_3 axes and C_2 axes, but antisymmetric with respect to the σ_d planes and S_4 axes. There is one doubly degenerate species E and two triply degenerate species F_1 and F_2.

Figure 2.2 shows the normal vibrations of a tetrahedral CH_4 molecule. ν_1 belongs to A_1 species, ν_{2a} and ν_{2b} belong to E species. Both $\nu_3(\nu_{3a}, \nu_{3b}, \nu_{3c})$ and $\nu_4(\nu_{4a}, \nu_{4b}, \nu_{4c})$ belong to F_2 species.

For degenerate vibrations, for example ν_{3a}, by carrying out the symmetry

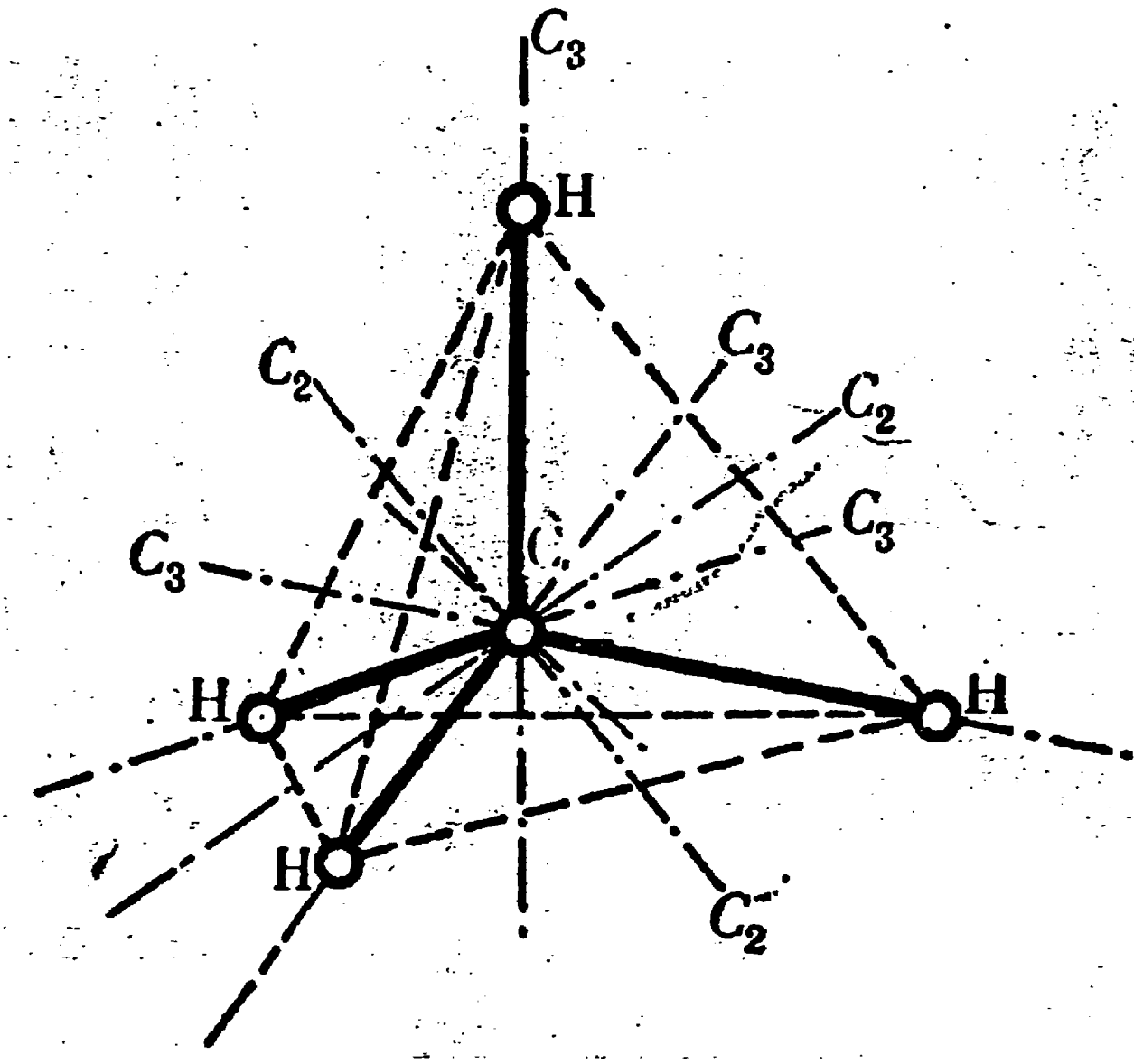

Figure 2.1: CH_4 Molecular Structure

Table 2.1: The Symmetry Type and the Characters for the Point Group T_d

T_d	I	$8C_3$	$6\sigma_d$	$6S_4$	$3S_4^2 \equiv 3C_2$	
O	I	$8C_3$	$6C_2$	$6C_4$	$3C_4^2 \equiv 3C_2''$	
A_1	+1	+1	+1	+1	+1	
A_2	+1	+1	−1	−1	+1	
E	+2	−1	0	0	+2	
F_1	+3	0	−1	+1	−1	T_x, T_y, T_z for O, R_x, R_y, R_z
F_2	+3	0	+1	−1	−1	T_x, T_y, T_z for T_d

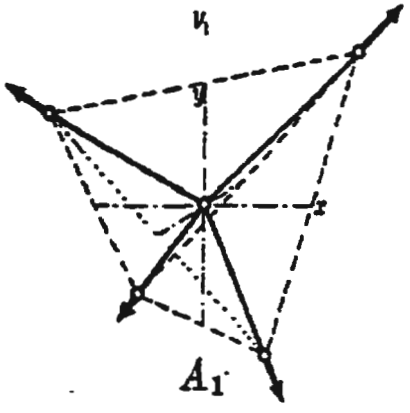
ν_1
y
x
z

A_1

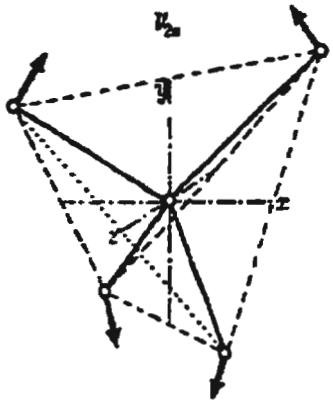
ν_{2a}
y
x
z

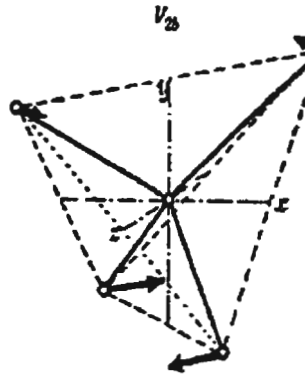
ν_{2b}
y
x
z

E

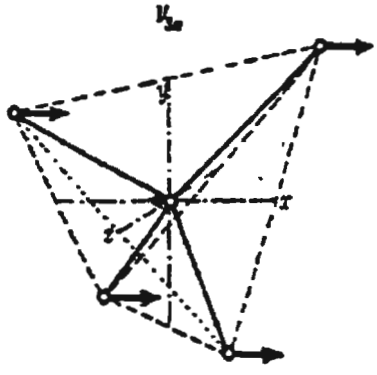
ν_{3a}
y
x
z

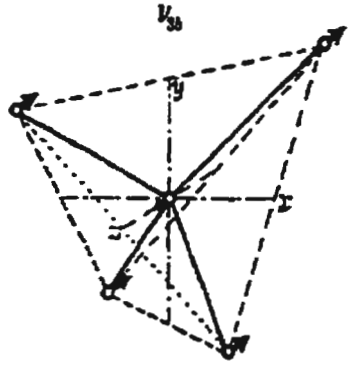
ν_{3b}
y
x
z

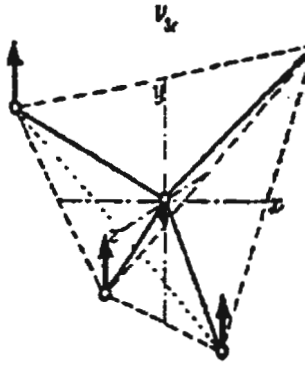
ν_{3c}
y
x
z

F_2

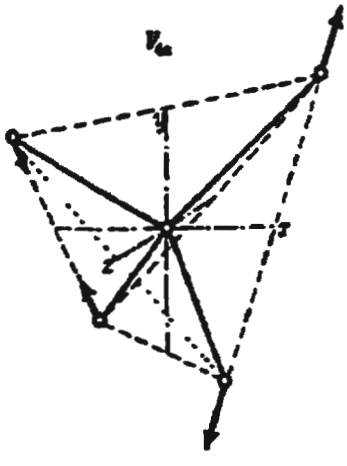
ν_{4a}
y
x
z

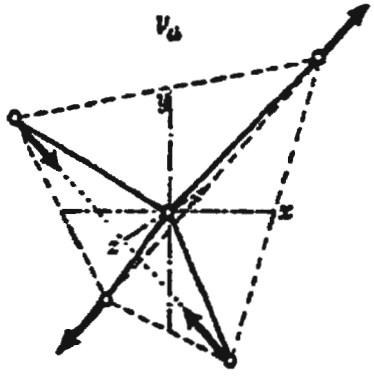
ν_{4b}
y
x
z

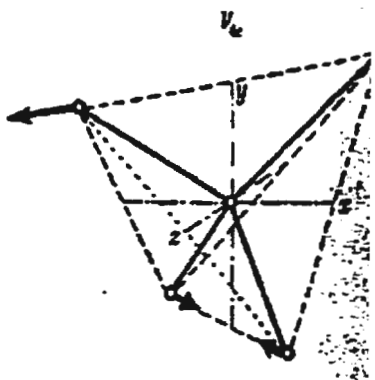
ν_{4c}
y
x
z

F_2

operations (for example, rotation about one of the C_3 axes), the vibration is transformed into a vibration that is, in general, a linear combination of the mutually degenerate vibrations.

For CH_4, there are no genuine normal vibrations of the species of A_2 and F_1, but the eigenfunctions of higher vibrational levels may belong to these species.

The frequencies ν_1, ν_2, ν_3, and ν_4 of CH_4 in gas state[18, 19, 20, 21, 22] are $2914.2cm^{-1}$, $1526cm^{-1}$, $3020.3cm^{-1}$, and $1306.2cm^{-1}$ respectively.

All four fundamental frequencies $(\nu_1, \nu_2, \nu_3, \nu_4)$ are allowed in the Raman effect (next Chapter), but only ν_3 and ν_4 are permitted in the infrared.

2.3 Solid CH_4

The triple point of CH_4 is 90.7K [23]. CH_4 has two phases at low pressure, phase I and phase II. The phase transition temperature is 20.4 K [24, 25]. The low temperature phase, phase II, is partially orientational ordered [26, 27, 28]. The high temperature phase, phase I, is probably orientationally disordered [29].

X-ray studies on crystalline CH_4 have shown that both phase I and phase II have face centered cubic (FCC) lattice structure.

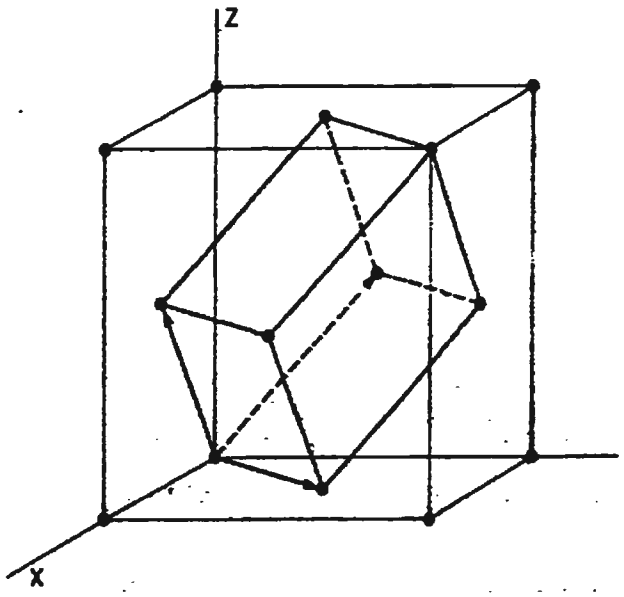

Figure 2.3: FCC Structure

Figure 2.3 shows the FCC structure (without considering orientational

ordering). Each molecule is surrounded by twelve molecules at an equal distance R_0 from the central molecule. These molecules are called the nearest neighbours (nn) of the central molecules.

The FCC lattice contains one molecule per primitive unit cell (without considering orientational ordering) and can be generated by the primitive vectors

$$\vec{a_1} = a(\hat{i} + \hat{j}),\ \vec{a_2} = a(\hat{j} + \hat{k}),\ \vec{a_3} = a(\hat{k} + \hat{i}) \tag{2.20}$$

where $a = R_0/2^{\frac{1}{2}}$ and $\hat{i}, \hat{j}, \hat{k}$ are unit vectors along the axes of a rectangular frame (Figure 2.3). The lattice points are then located at

$$\vec{R_l} = l_1\vec{a_1} + l_2\vec{a_2} + l_3\vec{a_3} \tag{2.21}$$

where $l_i = 0, \pm 1, \pm 2, ...$

Figure 2.4 shows the crystal structure of phase II, established by Press [26, 27, 28]. It belongs to space group O_h^6(Fm3c). In this structure there are eight molecules per primitive cell of which six (occupying sites of D_{2d} symmetry) are ordered, and two (occupying sites of O symmetry) are free to rotate.

In the crystal, there are two types of vibrations: internal and external vibrations [33]. External vibrations involve partial rotations and translations of molecules as a whole in the crystal lattice. Internal vibrations involve the stretching and bending, etc., of chemical bonds in the molecule (i.e. vibrations that are analagous with gas-phase vibrations). Since the potential energy of a molecule in a solid has been perturbed by the presence of other molecules in the crystal lattice, the frequency, degeneracy, and activity of

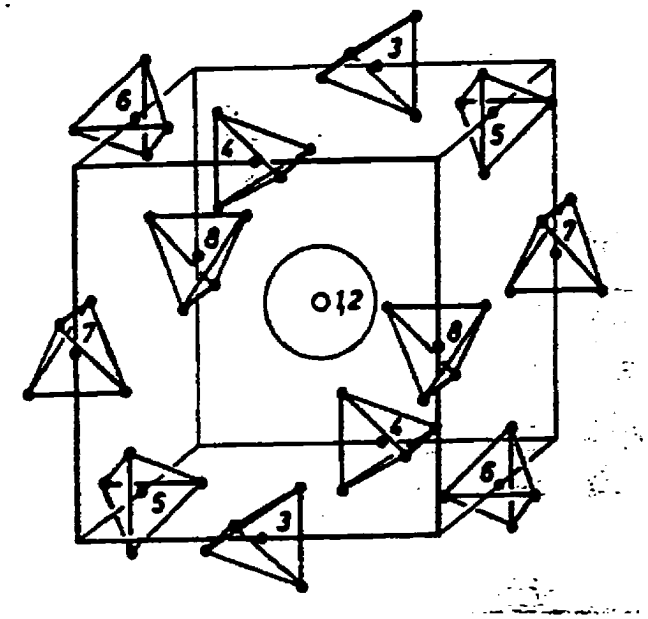

Figure 2.4: The Crystal Structure of Phase II for CH_4

internal vibration may change compared to those in the gaseous state. In this thesis, we study the ν_1 internal vibration in crystal CH_4.

Chapter 3

Vibrational Raman Spectra

3.1 Raman Effect

When the incident light quantum $h\nu'$ collides with a molecule, it can be scattered elastically or inelastically. The elastically scattered light, having the same frequency with the incident light, is called the Rayleigh line. The inelastically scattered light is the Raman spectrum. In the Raman process, the incident light can either give a part of its energy to the scattering system or take energy from the system, and the system changes from its initial state E'' to its final state E'. Let $\Delta E = |E' - E''|$, then if the system is initially in the lower state, the light quantum after scattering is $h\nu' - \Delta E$ (stokes lines). If the system is initially in the higher state, the light quantum after scattering is $h\nu' + \Delta E$ (anti-stokes lines).

Figure 3.1 illustrates the Raman bands for a given vibrational-rotation transition.

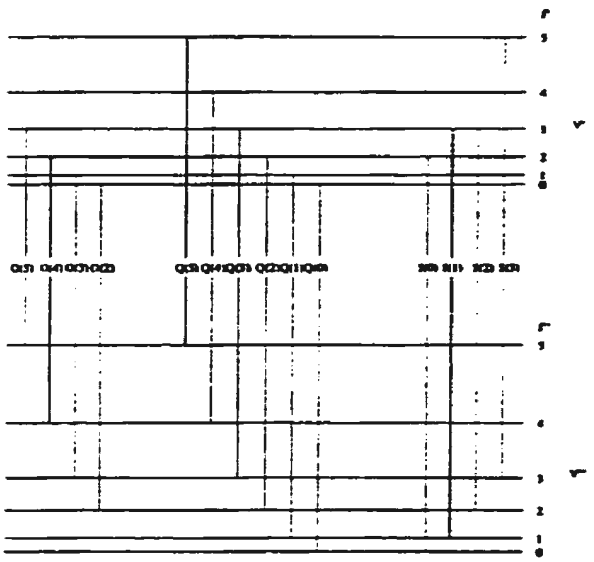

Figure 3.1: The Raman Bands

The intensity of Raman light depends on [16]

$$\int \Psi_n \vec{p} \Psi_m^* d\tau, \tag{3.1}$$

where $\vec{p}$ is induced dipole moment, and is written as

$$\vec{p} = \alpha \vec{E}. \tag{3.2}$$

Here α is the polarizability (a tensor), and $\vec{E}$ the electric vector of the incident light.

The time-independent part of equation 3.1 is

$$[\vec{p^0}]^{nm} = \int \psi_n \vec{p^0} \psi_m^* d\tau, \tag{3.3}$$

where $\vec{p^0}$ is the amplitude of $\vec{p}$.

The intensity of Raman transition $n \leftrightarrow m$ is proportional to the square of $[\vec{p^0}]^{nm}$, whose x, y, and z components are written as

$$[p_x^0]^{nm} = E_x^0[\alpha_{xx}]^{nm} + E_y^0[\alpha_{xy}]^{nm} + E_z^0[\alpha_{xz}]^{nm}$$

$$[p_y^0]^{nm} = E_x^0[\alpha_{xy}]^{nm} + E_y^0[\alpha_{yy}]^{nm} + E_z^0[\alpha_{yz}]^{nm}$$

$$[p_z^0]^{nm} = E_x^0[\alpha_{xz}]^{nm} + E_y^0[\alpha_{yz}]^{nm} + E_z^0[\alpha_{zz}]^{nm}, \tag{3.4}$$

where

$$[\alpha_{xx}]^{nm} = \int \alpha_{xx}\psi_n\psi_m^* d\tau, \ [\alpha_{xy}]^{nm} = \int \alpha_{xy}\psi_n\psi_m^* d\tau, \ \ldots \tag{3.5}$$

are the matrix elements of the six components of the polarizability tensor. The diagonal matrix elements (n=m) of α or $\vec{p^0}$ correspond to Rayleigh scattering, the off-diagonal elements correspond to Raman scattering (transition $n \leftrightarrow m$ induced by the incident light). According to equation 3.4, a Raman transition $n \leftrightarrow m$ is allowed if at least one of the six quantities $[\alpha_{xx}]^{nm}, [\alpha_{xy}]^{nm}, \ldots$, is different from zero.

For the vibrational Raman spectrum, the selection rule may also be stated in the following form: A Raman transition between two vibrational levels v' and v'' is allowed if the product $\psi_v'\psi_v''$ has the same species as at least one of the six components $\alpha_{xx}, \alpha_{xy}, \ldots$, of the polarizability tensor.

Table 3.1 gives the species of the six components of the polarizability tensor for some important point group. From this table, we can see that all ν_1, ν_2, ν_3 and ν_4 vibration of $CH_4(T_d)$ are Raman active as fundamentals.

	C_s	C_i	C_{2h} $[C_2]^1$	C_{2v}	$V_h \equiv D_{2h}$ $[V \equiv D_2]^1$	C_{3v}	C_{4v}	C_{5v} C_{6v}	C_∞
M_x	A'	A_u	B_u	B_1	B_{3u}	E	E	E_1	Π
M_y	A'	A_u	B_u	B_2	B_{2u}	E	E	E_1	Π
M_z	A''	A_u	A_u	A_1	B_{1u}	A_1	A_1	A_1	Σ^-
α_{xx}	A'	A_g	A_g	A_1	A_g	A_1, E	A_1, B_1	A_1, E_2	Σ^+
α_{yy}	A'	A_g	A_g	A_1	A_g	A_1, E	A_1, B_1	A_1, E_2	Σ^+
α_{zz}	A'	A_g	A_g	A_1	A_g	A_1	A_1	A_1	Σ^+
α_{xy}	A'	A_g	A_g	A_2	B_{1g}	E	B_2	E_2	Δ
α_{xz}	A''	A_g	B_g	B_1	B_{2g}	E	E	E_1	Π
α_{yz}	A''	A_g	B_g	B_2	B_{3g}	E	E	E_1	Π
	D_3 $[C_3]^2$	D_4 $[C_4]^2$	D_5 $[C_5]^2$	D_6 $[C_6]^2$	D_{3h} $[C_{3h}]^2$	D_{4h} $[C_{4h}]^2$	D_{5h} $[C_{5h}]^2$	D_{6h} $[C_{6h}]^2$	$D_{\infty h}$
M_x	E	E	E_1	E_1	E'	E_u	E_1'	E_{1u}	Π_u
M_y	E	E	E_1	E_1	E'	E_u	E_1'	E_{1u}	Π_u
M_z	A_2	A_2	A_2	A_2	A_2''	A_{2u}	A_2''	A_{2u}	Σ_u^-
α_{xx}	A_1, E	A_1, B_1	A_1, E_2	A_1, E_2	A_1', E'	A_{1g}, B_{1g}	A_1', E_2'	A_{1g}, E_{2g}	Σ_g^+, Δ_g
α_{yy}	A_1, E	A_1, B_1	A_1, E_2	A_1, E_2	A_1', E'	A_{1g}, B_{1g}	A_1', E_2'	A_{1g}, E_{2g}	Σ_g^+, Δ_g
α_{zz}	A_1	A_1	A_1	A_1	A_1'	A_{1g}	A_1'	A_{1g}	Σ_g^+
α_{xy}	E	B_2	E_2	E_2	E'	B_{2g}	E_2'	E_{2g}	Δ_g
α_{xz}	E	E	E_1	E_1	E''	E_g	E_1''	E_{1g}	Π_g
α_{yz}	E	E	E_1	E_1	E''	E_g	E_1''	E_{1g}	Π_g
	$D_{2d} \equiv V_d$	D_{3d}	D_{4d}	S_4	S_6	T_d $[T]^3$	O_h $[O]^4$		
M_x	E	E_u	E_1	E	E_{1u}	F_2	F_{1u}		
M_y	E	E_u	E_1	E	E_{1u}	F_2	F_{1u}		
M_z	B_2	A_{2u}	B_2	A	B_u	F_2	F_{1u}		
α_{xx}	A_1, B_1	A_{1g}, E_g	A_1, E_2	A,B	A_g, E_{2g}	A_1, E	A_{1g}, E_g		
α_{yy}	A_1, B_1	A_{1g}, E_g	A_1, E_2	A,B	A_g, E_{2g}	A_1, E	A_{1g}, E_g		
α_{zz}	A_1	A_{1g}	A_1	A	A_g	A_1, E	A_{1g}, E_g		
α_{xy}	B_2	E_g	E_2	B	E_{2g}	F_2	F_{2g}		
α_{xz}	E	E_g	E_3	E	E_{2g}	F_2	F_{2g}		
α_{yz}	E	E_g	E_3	E	E_{2g}	F_2	F_{2g}		

Table 3.1: Symmetry Types (Species) of the Components of the Dipole Moment and of the Polarizability for Some Important Point Groups

1. For C_2 and $D_2 \equiv V$ omit the subscripts g and u.
2. For C_3, C_4, C_5, C_6 and C_{3h}, C_{4h}, C_{5h}, C_{6h}, omit the subscripts 1 and 2 of A and B.
3. For T omit the subscripts 1 and 2 of A and F.
4. For O omit the subscripts g and u.

3.2 Raman Depolarization Ratio

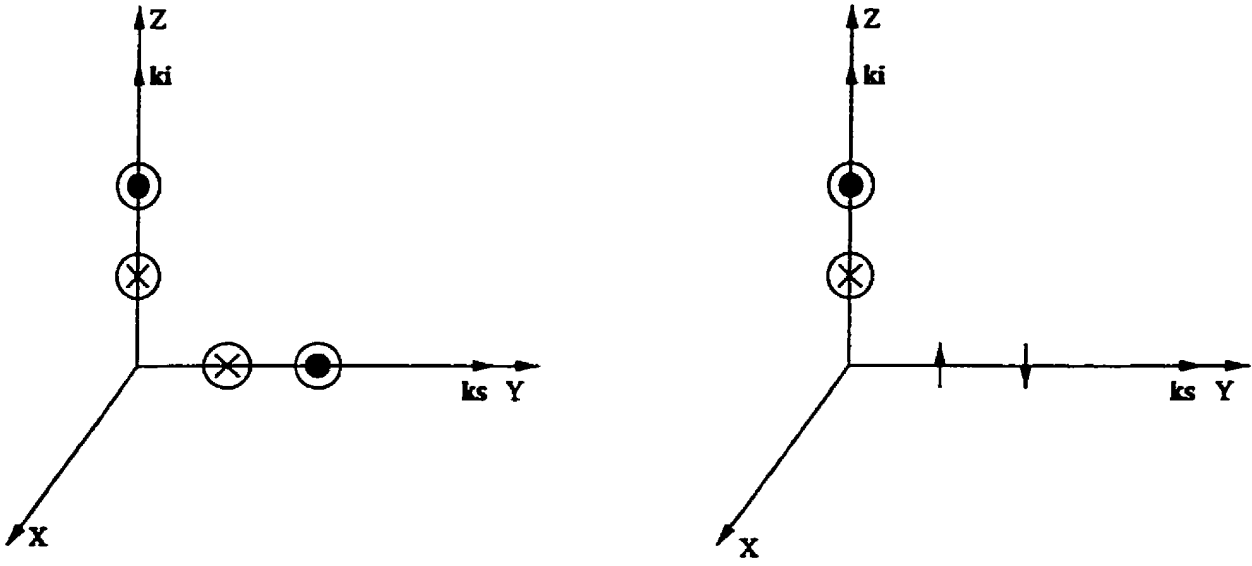

(a) Z(XX)Y case (b) Z(XZ)Y case

Figure 3.2: Polarization Properties of Raman Scattered Light (for $\theta = 90^0$)

Figure 3.2 shows the geometry of our experiment. The incident light propagates in the Z direction and is polarized in the X direction. We measure the Raman scattered light in Y direction. There are two cases. In case(a), Z(XX)Y case (the convention of Damen, Porto, and Tell) [31, 32], we measure the X polarization component of the scattered light. In case(b), Z(XZ)Y case, the Z polarization component of the scattered light is measured.

The intensities I_{XX} and I_{XZ} for Z(XX)Y and Z(XZ)Y cases [32, 33, 34] are

$$I_{XX} = K(\frac{\partial \alpha_{XX}}{\partial Q_j})^2 \propto (\frac{\partial \alpha_{XX}}{\partial Q_j})^2 \tag{3.6}$$

$$I_{XZ} = K(\frac{\partial \alpha_{ZX}}{\partial Q_j})^2 \propto (\frac{\partial \alpha_{ZX}}{\partial Q_j})^2, \tag{3.7}$$

where

$$K = \frac{8A}{c^4 \nu_0'}(\nu - \nu')^4 E^2 \frac{1}{(1 - e^{-h\nu'/KT})} K_2(instrument)$$

The Raman depolarization ratio (degree of depolarization) ρ is

$$\rho = \frac{I_{XZ}}{I_{XX}} = (\frac{\partial \alpha_{ZX}}{\partial Q_j})^2 / (\frac{\partial \alpha_{XX}}{\partial Q_j})^2 \tag{3.8}$$

In crystal coordinate system (x,y,z), the polarizability derivative of crystal can be written as

$$\frac{\partial \alpha_{cry}}{\partial Q_j} = \begin{pmatrix} a_{11} & a_{12} & a_{13} \\ a_{21} & a_{22} & a_{23} \\ a_{31} & a_{32} & a_{33} \end{pmatrix} \tag{3.9}$$

$$a_{ij} = a_{ji}$$

In laboratory coordinate system (space fixed system XYZ)

$$\frac{\partial \alpha_{lab}}{\partial Q_j} = R \begin{pmatrix} a_{11} & a_{12} & a_{13} \\ a_{21} & a_{22} & a_{23} \\ a_{31} & a_{32} & a_{33} \end{pmatrix} R^{-1} \tag{3.10}$$

$$(\frac{\partial \alpha_{lab}}{\partial Q_j})_{ij} = \sum_{ml} R_{im} a_{ml} R_{jl} \tag{3.11}$$

where R is the rotational matrix and given by

$$R = \begin{pmatrix} cos\chi cos\phi - cos\theta sin\phi sin\chi & -sin\chi cos\phi - cos\theta sin\phi cos\chi & sin\theta sin\phi \\ cos\chi sin\phi + cos\theta cos\phi sin\chi & -sin\chi sin\phi + cos\theta cos\phi cos\chi & -sin\theta cos\phi \\ sin\chi sin\theta & cos\chi sin\theta & cos\theta \end{pmatrix} \tag{3.12}$$

Here θ, ϕ and χ are Euler angles of the crystal.

Let

$$s_1 = \frac{a_{11}}{a_{11}} = 1,\ s_2 = \frac{a_{22}}{a_{11}},\ s_3 = \frac{a_{33}}{a_{11}},\ s_4 = \frac{a_{23}}{a_{11}},\ s_5 = \frac{a_{31}}{a_{11}},\ s_6 = \frac{a_{12}}{a_{11}}. \quad (3.13)$$

Then from equation 3.8 to 3.13, we can get

$$\rho = \frac{(c_{t1} + \sum_{i=2}^{6} c_{ti}s_i)^2}{(c_{b1} + \sum_{i=2}^{6} c_{bi}s_i)^2} \quad (3.14)$$

where

$$c_{b1} = R_{11}^2;\ c_{t1} = R_{11}R_{31};\ c_{b2} = R_{12}^2;\ c_{t2} = R_{12}R_{32};\ c_{b3} = R_{13}^2;$$

$$c_{t3} = R_{13}R_{33};\ c_{b4} = 2R_{12}R_{13};\ c_{t4} = R_{12}R_{33} + R_{13}R_{32};\ c_{b5} = 2R_{11}R_{13};$$

$$c_{t5} = R_{11}R_{33} + R_{13}R_{31};\ c_{b6} = 2R_{11}R_{12};\ c_{t6} = R_{11}R_{32} + R_{12}R_{31} \quad (3.15)$$

In our experiment, we first determine the orientation (θ, ϕ, χ) of the crystal CH_4, then change ϕ for each temperature T, and measure $\rho(\phi)$. From these experimental data, we can use nonlinear least squares methods to get s_2, s_3, s_4, s_5, s_6.

If we assume the principal axes are along the C_4 axes of the crystal, then

$$\frac{\partial \alpha_{cry}}{\partial Q_j} = \begin{pmatrix} a_{11} & 0 & 0 \\ 0 & a_{22} & 0 \\ 0 & 0 & a_{33} \end{pmatrix} \quad (3.16)$$

Equation 3.14 can be simplified to

$$\rho = \frac{(c_{t1} + \sum_{i=2}^{3} c_{ti}s_i)^2}{(c_{b1} + \sum_{i=2}^{3} c_{bi}s_i)^2} \quad (3.17)$$

In this work, we will try to test whether or not this assumption is satisfied.

3.3 The Effect of Molecular Orientations

In molecular coordinate system $x'y'z'$, the derived polarizability tensor of the molecule is α'_{mol}. If the orientation of the molecule in space fixed coordinate system (laboratory system XYZ) is θ, ϕ, χ, then [35]

$$\alpha'_{lab} = R(\theta, \phi, \chi)\alpha'_{mol}R^{-1}(\theta, \phi, \chi) \tag{3.18}$$

For a substance in which molecular orientation is perfectly random, the Raman depolarization ratio may be expressed in terms of following two invariants of the derived polarizability tensor [16]:

$$\alpha'^{I} = \frac{1}{3}(\alpha'_{11} + \alpha'_{22} + \alpha'_{33}) \tag{3.19}$$

$$\beta'^{2} = \frac{1}{2}[(\alpha'_{11} - \alpha'_{22})^2 + (\alpha'_{22} - \alpha'_{33})^2 + (\alpha'_{33} - \alpha'_{11})^2 + 6(\alpha'^{2}_{12} + \alpha'^{2}_{23} + \alpha'^{2}_{31})] \tag{3.20}$$

where α'_{ij} are elements of the derived tensor (in molecular coordinate system $x'y'z'$)

$$\rho_n = \frac{6\beta'^{2}}{45(\alpha'^{I})^2 + 7\beta'^{2}} \tag{3.21}$$

$$\rho_l = \frac{\rho_n}{2 - \rho_n} \tag{3.22}$$

where subscripts n and l indicate natural (unpolarized) and linearly polarized incident light respectively.

The maximum values for the random orientation case are

$$\rho_n^{max} = \frac{6}{7}, \quad and \quad \rho_l^{max} = \frac{3}{4}. \tag{3.23}$$

If the incident light is elliptically polarized, it can be shown that the maximum value of the Raman depolarization ratio ($\rho_{ell} = (I_{XZ} + I_{YZ})/(I_{XX} + I_{YX})$) for random orientation case is $\rho_{ell}^{max} = 1$.

If the molecular orientations are not perfectly random, the depolarization ratio ρ depends on the molecular orientations.

Figure 3.3 shows some cases of partial orientation. In case I, the molecular axis z' is parallel to one of space fixed axes (X or Y or Z). In case II, the z' axis is confined in a space fixed plane (XZ or YZ or XY).

By averaging over χ in case I, and over ϕ and χ in case II, we can calculate the quantities $\overline{\alpha'^2_{lab\ IJ}}$ (in space fixed system XYZ)

$$\overline{\alpha'^2_{lab\ IJ}} = \overline{(\sum_{ij} R_{Ii} R_{Jj} \alpha'_{ij})^2} \tag{3.24}$$

The polarizability derivatives for T_d symmetry are listed in table 3.2 [32]. From this table, we can get

$$\frac{\partial \alpha_{mol}}{\partial Q_{A_1}} = \begin{pmatrix} a & 0 & 0 \\ 0 & a & 0 \\ 0 & 0 & a \end{pmatrix}, \frac{\partial \alpha_{mol}}{\partial Q_{E_a}} = \begin{pmatrix} b & 0 & 0 \\ 0 & b & 0 \\ 0 & 0 & -2b \end{pmatrix}, \frac{\partial \alpha_{mol}}{\partial Q_{E_b}} = \begin{pmatrix} -\sqrt{3}b & 0 & 0 \\ 0 & \sqrt{3}b & 0 \\ 0 & 0 & 0 \end{pmatrix}$$

$$\frac{\partial \alpha_{mol}}{\partial Q_{F_{2a}}} = \begin{pmatrix} 0 & 0 & 0 \\ 0 & 0 & c \\ 0 & c & 0 \end{pmatrix}, \frac{\partial \alpha_{mol}}{\partial Q_{F_{2b}}} = \begin{pmatrix} 0 & 0 & c \\ 0 & 0 & 0 \\ c & 0 & 0 \end{pmatrix}, \frac{\partial \alpha_{mol}}{\partial Q_{F_{2c}}} = \begin{pmatrix} 0 & c & 0 \\ c & 0 & 0 \\ 0 & 0 & 0 \end{pmatrix} \tag{3.25}$$

where a,b and c are constants.

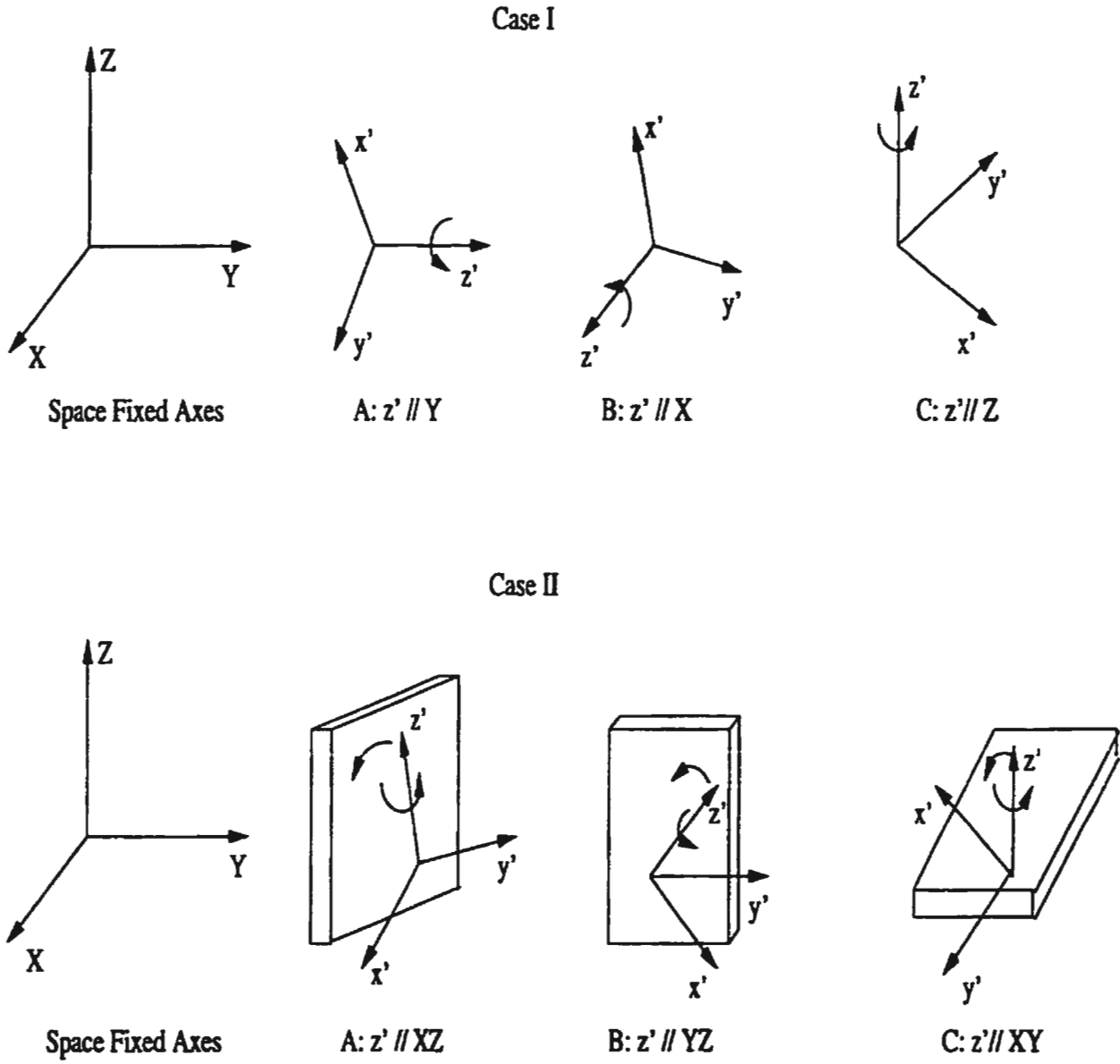

Figure 3.3: Some Cases of Partially Molecular Orientations

Table 3.2: The Symmetry Type and the Polarizability Derivatives for the Point Group T_d

O / T_d	E	$8C_3$	$3C_2$	$6C_4$	$6C_2'$		μ'_X	μ'_Y	μ'_Z	α'_{XX}	α'_{YY}	α'_{ZZ}	α'_{XY}	α'_{XZ}	α'_{YZ}
	E	$8C_3$	$3C_2$	$6S_4$	$6\sigma_d$										
A_1	1	1	1	1	1		0	0	0	a	a	a	0	0	0
A_2	1	1	1	−1	−1		0	0	0	0	0	0	0	0	0
E	2	−1	2	0	0		0	0	0	b	b	$-2b$	0	0	0
							0	0	0	$-3^{1/2}b$	$3^{1/2}b$	0	0	0	0
F_1	3	0	−1	1	−1	$T_X(O); R_X$	$l(O)$	0	0	0	0	0	0	0	0
						$T_Y(O); R_Y$	0	$l(O)$	0	0	0	0	0	0	0
						$T_Z(O); R_Z$	0	0	$l(O)$	0	0	0	0	0	0
F_2	3	0	−1	−1	1	$T_X(T_d)$	$l(T_d)$	0	0	0	0	0	0	0	c
						$T_Y(T_d)$	0	$l(T_d)$	0	0	0	0	0	c	0
						$T_Z(T_d)$	0	0	$l(T_d)$	0	0	0	c	0	0

We calculated the $\overline{\alpha'^2_{labXX}}, \overline{\alpha'^2_{labXZ}}, \overline{\alpha'^2_{labYX}}, \overline{\alpha'^2_{labYZ}}$ and the depolarization ratio for six different partial orientations (Figur 3.3) of T_d type molecule using equations 3.24 and 3.25. The calculated results are listed in table 3.3 and table 3.4.

In our experiments, the polarization of incident light E_i is in the X direction, so in table 3.4 we only give the results of ρ for this situation.

From table 3.4, we can see that if the molecular axis is parallel to one of the laboratory axes X or Z, or confined on the YZ plane, the depolarization ratio for F_2 species will be ∞.

J.Zhao and R.L.McCreery measured the Raman depolarization ratio ρ for $CoPc$ (D_{4h} group) on carbon surfaces [36]. Their experimental results are consistent with the results calculated from equation 3.24. For some mode, they observed very large depolarization ratio ρ (> 6).

Table 3.3: Raman Scattering Activities (T_d, I = X or Y)

Sample	*Species*	E_i	*Polarization of Raman Radiation*					
			A(z'// Y)		B(z'// X)		C(z'// Z)	
			$X(\overline{\alpha'^2_{IX}})$	$Z(\overline{\alpha'^2_{IZ}})$	$X(\overline{\alpha'^2_{IX}})$	$Z(\overline{\alpha'^2_{IZ}})$	$X(\overline{\alpha'^2_{IX}})$	$Z(\overline{\alpha'^2_{IZ}})$
Case I	A_1	X	a^2	0	a^2	0	a^2	0
	A_1	Y	0	0	0	0	0	0
	E_a	X	b^2	0	$4b^2$	0	b^2	0
	E_a	Y	0	0	0	0	0	0
	E_b	X	$\frac{3}{2}b^2$	$\frac{3}{2}b^2$	0	0	$\frac{3}{2}b^2$	0
	E_b	Y	0	0	0	$\frac{3}{2}b^2$	$\frac{3}{2}b^2$	0
	F_{2a}	X	0	0	0	$\frac{1}{2}c^2$	0	$\frac{1}{2}c^2$
	F_{2a}	Y	$\frac{1}{2}c^2$	$\frac{1}{2}c^2$	$\frac{1}{2}c^2$	0	0	$\frac{1}{2}c^2$
	F_{2b}	X	0	0	0	$\frac{1}{2}c^2$	0	$\frac{1}{2}c^2$
	F_{2b}	Y	$\frac{1}{2}c^2$	$\frac{1}{2}c^2$	$\frac{1}{2}c^2$	0	0	$\frac{1}{2}c^2$
	F_{2c}	X	$\frac{1}{2}c^2$	$\frac{1}{2}c^2$	0	0	$\frac{1}{2}c^2$	0
	F_{2c}	Y	0	0	0	$\frac{1}{2}c^2$	$\frac{1}{2}c^2$	0
			A(z'// XZ)		B(z'// YZ)		C(z'// XY)	
			$X(\overline{\alpha'^2_{IX}})$	$Z(\overline{\alpha'^2_{IZ}})$	$X(\overline{\alpha'^2_{IX}})$	$Z(\overline{\alpha'^2_{IZ}})$	$X(\overline{\alpha'^2_{IX}})$	$Z(\overline{\alpha'^2_{IZ}})$
Case II	A_1	X	a^2	0	a^2	0	a^2	0
	A_1	Y	0	0	0	0	0	0
	E_a	X	$\frac{19}{8}b^2$	$\frac{1}{8}b^2$	b^2	0	$\frac{19}{8}b^2$	0
	E_a	Y	0	0	0	$\frac{1}{8}b^2$	$\frac{1}{8}b^2$	0
	E_b	X	$\frac{9}{16}b^2$	$\frac{3}{16}b^2$	$\frac{3}{2}b^2$	$\frac{3}{4}b^2$	$\frac{9}{16}b^2$	$\frac{3}{4}b^2$
	E_b	Y	$\frac{3}{4}b^2$	$\frac{3}{4}b^2$	$\frac{3}{4}b^2$	$\frac{3}{16}b^2$	$\frac{3}{16}b^2$	$\frac{3}{4}b^2$
	F_{2a}	X	$\frac{1}{4}c^2$	$\frac{1}{4}c^2$	0	$\frac{1}{4}c^2$	$\frac{1}{4}c^2$	$\frac{1}{4}c^2$
	F_{2a}	Y	$\frac{1}{4}c^2$	$\frac{1}{4}c^2$	$\frac{1}{4}c^2$	$\frac{1}{4}c^2$	$\frac{1}{4}c^2$	$\frac{1}{4}c^2$
	F_{2b}	X	$\frac{1}{4}c^2$	$\frac{1}{4}c^2$	0	$\frac{1}{4}c^2$	$\frac{1}{4}c^2$	$\frac{1}{4}c^2$
	F_{2b}	Y	$\frac{1}{4}c^2$	$\frac{1}{4}c^2$	$\frac{1}{4}c^2$	$\frac{1}{4}c^2$	$\frac{1}{4}c^2$	$\frac{1}{4}c^2$
	F_{2c}	X	$\frac{3}{16}c^2$	$\frac{1}{16}c^2$	$\frac{1}{2}c^2$	$\frac{1}{4}c^2$	$\frac{3}{16}c^2$	$\frac{1}{4}c^2$
	F_{2c}	Y	$\frac{1}{4}c^2$	$\frac{1}{4}c^2$	$\frac{1}{4}c^2$	$\frac{1}{16}c^2$	$\frac{1}{16}c^2$	$\frac{1}{4}c^2$

Table 3.4: Theoretical Depolarization Ratio, ρ, of Different Types of Vibrations for Six Different Partial Orientations of a T_d Type Molecule

Case I	A(z'// Y)						B(z'// X)						C(z'// Z)				
Species	A_1	E_a	E_b	F_{2a}	F_{2b}	F_{2c}	A_1	E_a	E_b	F_{2a}	F_{2b}	F_{2c}	A_1	E_a	E_b	F_{2a}	F_2
ρ	0	0	1	×	×	1	0	0	×	∞	∞	×	0	0	0	∞	∞
Case II	A(z'// XZ)						B(z'// YZ)						C(z'// XY)				
Species	A_1	E_a	E_b	F_{2a}	F_{2b}	F_{2c}	A_1	E_a	E_b	F_{2a}	F_{2b}	F_{2c}	A_1	E_a	E_b	F_{2a}	F_2
ρ	0	$\frac{1}{19}$	$\frac{1}{3}$	1	1	$\frac{1}{3}$	0	0	$\frac{1}{2}$	∞	∞	$\frac{1}{2}$	0	0	$\frac{4}{3}$	1	
Case III	Random																
Species	A_1	E_a	E_b	F_{2a}	F_{2b}	F_{2c}											
ρ	0	$\frac{3}{4}$	$\frac{3}{4}$	$\frac{3}{4}$	$\frac{3}{4}$	$\frac{3}{4}$											

3.4 Lineshape Fitting

The observed spectra $F_{ob}(\nu)$ in experiments are the convolution of the laser spectra (instrument function) and the Raman spectra,

$$F_{ob}(\nu) = \int_{-\infty}^{\infty} F_{Las}(\nu') F_{Ram}(\nu - \nu') d\nu'. \tag{3.26}$$

According to the convolution theorem [37, 38],

$$\mathcal{F}\{F_{ob}(\nu)\} = \mathcal{F}\{F_{Las}(\nu)\}\mathcal{F}\{F_{Ram}(\nu)\}, \tag{3.27}$$

where $\mathcal{F}\{\}$ indicates Fourier transform.

If $F(x)$ is a real function in $(-l, +l)$, then it can be expanded into following Fourier series,

$$F(x) = \sum_{n=-\infty}^{\infty} c_n e^{i2\pi n f_1 x} = c_0 + \sum_{n=1}^{\infty} 2|c_n| cos(2\pi n f_1 x + arg c_n), \tag{3.28}$$

where

$$f_1 = \frac{1}{2l},$$

and

$$c_n = \frac{1}{2l}\int_{-l}^{+l} F(\xi)[e^{i\frac{n\pi}{l}\xi}]d\xi. \tag{3.29}$$

From equation 3.27 and equation 3.28, we get

$$c_{n,Ram} = \frac{c_{n,ob}}{c_{n,Las}} \tag{3.30}$$

or

$$|c_{n,Ram}| = \frac{|c_{n,ob}|}{|c_{n,Las}|}$$

$$arg(c_{n,Ram}) = arg(c_{n,ob}) - arg(c_{n,Las}) \tag{3.31}$$

We wrote a program to do the deconvolution based on equations 3.28 to 3.31.

Chapter 4

Experimental Arrangement

4.1 Experimental Setup

The experimental arrangement for Raman scattering studies of transparent single crystals and the laboratory coordinates (XYZ) are shown in Figure 4.1. A single mode Ar^+ laser beam was incident vertically along the axis of the sample cell – Z axis, and polarized in the X direction. The spectrometer consisted of a narrow band filter(F), a Fabry-Perot interferometry(FP), a photomutiplier tube(PMT), an amplifier discriminator(AD), and a data acquisition and stabilization system (computer). By rotating polarizer P2, the X and Z components could be measured. The reference laser beam was introduced by the beam splitters (BS1, BS2), the shutter (ST) and the fibre (FB). The He-Ne laser was used to define the optic axis – Y axis, and to do optical adjustment. The orientations of the crystals were determined by X-ray Laue transmission photographs.

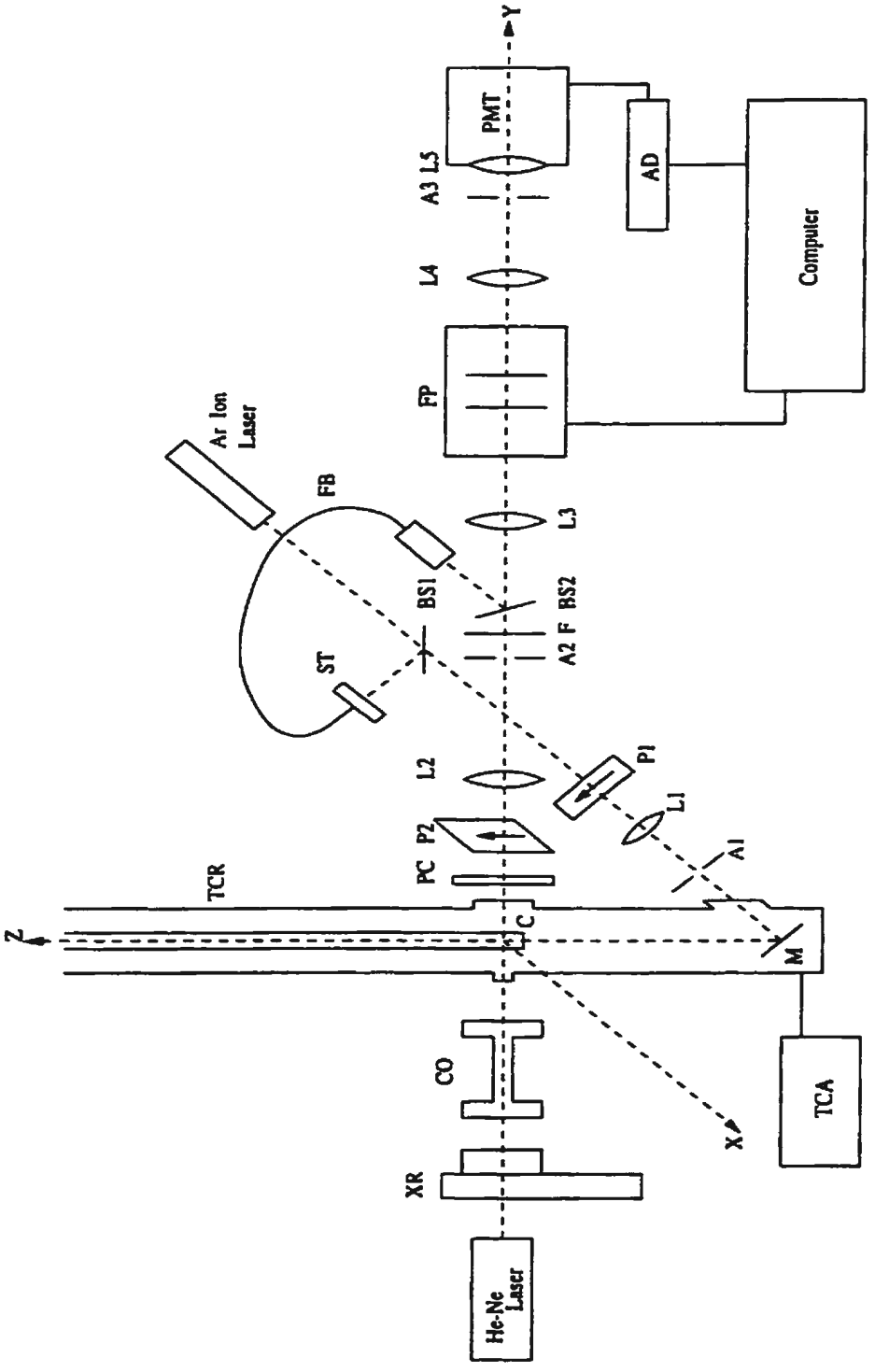

Figure 4.1: The Experimental Arrangement

Figure 4.1: The Experimental Arrangement

4.2 Laser

The laser light used in the experiments was generated from a Coherent Innova 90 Argon Ion Laser. The wavelength of the output was selected to 514.5 nm by adjusting the intracavity prism. The selected line had a line width of 10 GHz, which consisted of several modes separated about 150 MHz from each other. A single-mode was obtained by using an (Fabry-Perot) intracavity etalon. The etalon was housed in a temperature controlled mount to minimize frequency drift.

The frequency stability of the laser depends on temperature changes of the cavity length, mechanical shifts and 'jitter' [39, 40]. The laser was mounted on a steel table bearing a large granite block. The water supply to the laser was flow-regulated to decrease temperature changes and vibrations. A 'jitter' of 10-15 MHz, mainly caused by the flow of cooling water, was always present in this experiment. The laser power was reduced to 10 mW by an attenuator to avoid destroying the crystals by heating effects.

4.3 Fabry-Perot Interferometer

The Fabry-Perot interferometer (which was previously constructed at MUN) consists of two parallel plates (mirrors) separated by a distance d [39, 40, 41]. The inner surfaces of the plates are flat to $\lambda/200$ (at $\lambda = 500\ nm$) and are coated with highly reflective (98%) films. The front plate is manually adjustable by three micrometer screws. The rear plate is mounted on three piezoelectric transducers. When a beam of light is incident on the Fabry-Perot interferometer, only those wavelengths which satisfy the constructive interference condition are transmitted. The condition for constructive interference is

$$2ndcos\theta = m\lambda, \tag{4.1}$$

where

n = refractive index of the medium between the plates,

θ = the angle between the incident ray and the normal to the plates,

m = order of interference,

λ = wavelength of incident light.

In our experimentts, θ was equal to or very close to zero. Then, the condition 4.1 reduces to

$$2nd = m\lambda.$$

Thus, different wavelengths can be passed (scanned) by changing d as described in Section 4.4.

The range of wavelengths which can be displayed between two consecutive orders is called the free spectral range (FSR).

Assuming that the spectrum of (m-1)th order for λ_2 overlaps with the spectrum of the mth order for λ_1, then

$$2d = m\lambda_1 = (m-1)\lambda_2 \tag{4.2}$$

$$\Delta\lambda = \lambda_2 - \lambda_1 = \frac{\lambda_2}{m} = \frac{\lambda_1\lambda_2}{2d}$$

Because λ_1 and λ_2 are very close, $\lambda_2 \approx \lambda_1 = \lambda$, then

$$\Delta\lambda = \frac{\lambda^2}{2d}. \tag{4.3}$$

Expressing equation 4.3 in frequency units, we get the convenient equation for FSR

$$FSR = \Delta\nu = \frac{c}{\lambda^2}\Delta\lambda = \frac{c}{2d} \tag{4.4}$$

The FSR required in the Raman study is relatively high (800GHz – 900GHz). The corresponding distance d is small (0.167mm – 0.188mm), and not easy to measure accurately. We used a dye laser to calibrate the Fabry-Perot interferometer. We chose different known wavenumbers for the output of the dye laser, and got the relationship between the wavenumber and the peak position (channel number). The relationship is linear as shown in Figure 4.2. From the slope and the value of channel difference for one whole order, we got the estimated value of FSR. Then, we calculated the

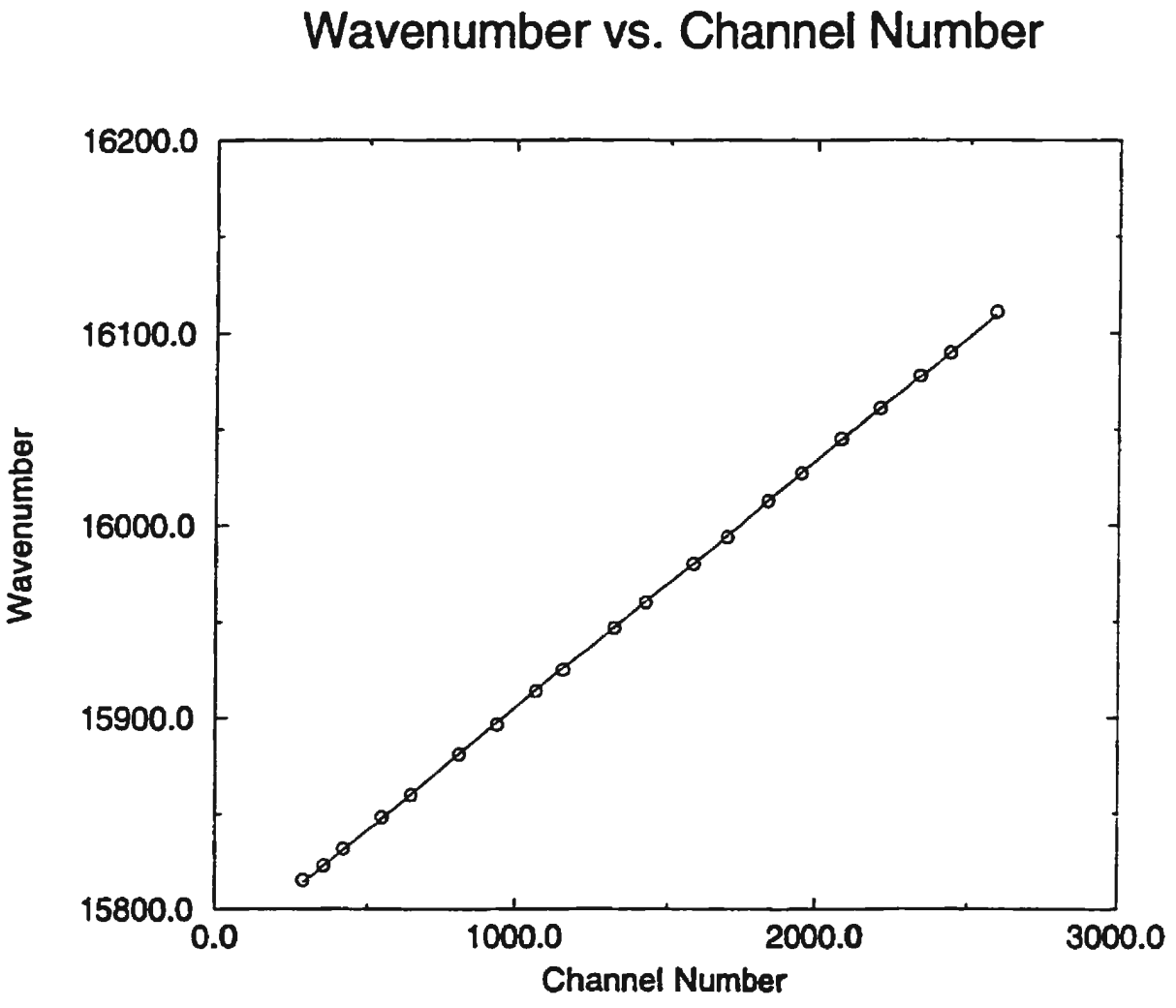

Figure 4.2: The Relationship Between the Wavenumber and the Channel Number

wavenumber needed for jumping some whole number of orders (eg. 8 orders), and checked it by jumping such order. By this method, the FSR was determined to be 884.2 GHz±0.1 GHz.

The finesse, F, of the Fabry-Perot is defined as the ratio between the FSR and the minimum resolvable bandwidth ($\Delta\nu_{min}$), which is arbitrarily chosen as the full width at half the maximum intensity.

$$F = \frac{FSR}{FWHM} \tag{4.5}$$

The higher the finesse, the greater the ability to resolve closely-spaced lines. The value of the finesse is affected by the reflectivity and the flatness of the mirrors, and the diffraction at pinhole A3.

The contrast is defined as the ratio of transmission maxima to transmission minima,

$$C_1 = \frac{t_{max}}{t_{min}} = \frac{4F_1^2}{\pi^2} \tag{4.6}$$

which, in other words, means the ability to detect small signals in the presence of large signals.

In our experiments, we used a single-pass FP interferometer. The diameter D of A3 is 0.8 mm. The finesse was about 40 and contrast was about 10^2.

4.4 Data Aquisition and Stabilization System

The data acquisition and control (DACS) is achieved by a IBM PC computer. The package is made up of an IBM PC plug-in card, a DDA-06 analog/digital expansion board and associated software. This system was designed and developed at MUN by O. Vazquez. The DACS performed several functions:

a) It stored digital data generated by the phototube (PMT) and the amplifier/discriminator (AD), and displayed the resultant spectrum on the monitor of the computer. The maximum channel number could be chosen from 640, 1280, ..., to 3840. In our experiments, we used 640 channels.

b) It produced the ramp signals, which were amplified by a high voltage amplifier and then applied to the three piezoelectric transducers to scan the rear mirror of the Fabry-Perot interferometer. The clock generated a series of pulses (ramp signals) of equal magnitude and duration, which were amplified and integrated to about 1000V by the high voltage amplifier and supplied to the piezoelectric elements. The clock also addressed the channel address scaler of the multi-channel analyzer. There was a one-to-one correspondence between the voltage, the channel number, and the frequency. The time spent in every channel in one sweep could be chosen in the range of 50 μs to 65535 μs.

c) A drift stabilization system was incorporated to correct for the frequency drifts due to temperature changes in the laser cavity and the Fabry-Perot cavity. If the ratio of the difference between the position of the peak of

the reference light and the reference channel (channel 60 in our experiments) to the width of the reference window ($\sim$ 10 channel) is more than the preset value (eg. 30%), a correction voltage was automatically applied to the ramp scaler (during flyback) to bring the peak back towards the reference channel.

d) The DACS also maximized the finesse. The finesse optimizer compared the counts in the control window for the current and previous sweep. If the difference was larger than the preset percentage (eg. 30%), the finesse correction would be excecuted to adjust the parallelism of the mirrors, and therefore to maximize the finesse.

e) The segmented-time-base feature of the DACS allowed for spending more time ($1 - 65535$ times more) in accumulating counts in selected regions of the spectrum. This is very important when studying weakly spectral features.

4.5 Alignment

The optical arrangment, as shown in Figure 4.1, was similar to that of references [39, 40], except that we put the shutter (ST), beam splitters (BS1,BS20), and the fibre into the arrangement.

The He-Ne laser beam defined the horizontal optic axis – Y axis of the laboratory coordinates. The Z axis was defined along the vertical axis of the cell. The incident argon-ion laser beam was made to translate along the Z-axis by adjusting the lens L1 and the mirror (prism) M which deflected the beam upwards. The purpose of aperture A1 was to block unwanted light from entering the cell. By adjusting the lens L1, the argon-ion laser beam in the cell could be made to coincide with the Z axis. A pentaprism was used to ensure that the argon-ion and the He-Ne laser beams were perpendicular to each other within 15' error. The polarizer P1 was used to make sure that the argon-ion laser light was polarized in Z direction before it entered the prism M. After the reflection from the prism M, the laser beam was polarized in X direction. The lens L2 produced an image of the origin (the intersection of the Y axis and the Z axis in the cell) at the position of the narrow band filter F. The band pass of the filter F was 605 nm±5 nm. The lens L3 was focused on the image produced by L2 (the position of F). The parallel rays from L3 were then incident on the Fabry-Perot interferometer (FP). The output of the Fabry-Perot was focused onto a pinhole A3 (0.8mm) by the lens L4. The light passing through the pinhole was collected by the lens L5 and focussed on to the photocathode of the photomultiplier tube (PMT). The photomultiplier tube (PMT) was mounted in a thermoelectrically cooled RF shielded chamber which controlled the cathode temperature to $-20 \pm 0.5^{0}C$.

The output pulses from the PMT were fed into the amplifier/discriminator (AD) which separated the photopulses from the tube noise and produced a series of identical 1 volt pulses at a rate proportional to the intensity of the light incident on PMT. These pulses were the input signals of the data acquisition and stabilization system (computer). The dark count was about 3 counts/sec. The beam splitter BS1 was used to split a second laser beam which was then introduced into the Febry-Perot by the shutter ST, the fibre FB and the second beam splitter BS2. The second laser beam was used as reference. The shutter was controlled by the computer and only opened in a small range around the reference channel (60 ± 10 channel). The output end of the fibre was positioned at the focus of lens L3.

The alignment of the system was achieved as follows: First, we removed everything on the optic axis except apertures A2 and A3, and the photomultiplier tube PMT, and directed the He-Ne laser beam through A2 and A3. The position of the PMT was adjusted to make it centered and perpendicular to the direction of the beam. The X-ray collimator CO was then positioned and adjusted so that the beam passed exactly through the pinholes, thus making sure that the X-ray beam would also lie along the optic axis. Next, the FP was placed in position and levelled so that the laser beam entered and exited at the centre of its apertures. The Fabry-Perot mirrors were made perpendicular to the beam by making the back reflection from the front mirror to coincide with the He-Ne incident beam.

Lens L3 was now placed and adjusted so that it backreflected the beam on itself and sent a parallel beam through the Fabry-Perot. Lens L4 was

positioned so that the focussed beam was made to pass through the pinhole A3. The FP plates were made parallel by adjusting the fine screws of the front mirror while scanning the FP (at about 1 scan/sec) and observing the transmitted beam visually until a single flashing was observed in the plane of A3. Lens L2 was then placed and adjusted to backreflect the beam on it self. We now moved the cryostat into the system and turn on the Ar^+ laser beam so that the two laser beams intersected at axis of the sample cell at 3 mm above the bottom of the cell. Filter F was put in the position of the focus point of L3 and the position of L2 was adjusted to produce the image of the cell at the filter (removing A2). The cryostat was then moved away and replaced by the white card. The front mirror of the FP was adjusted by observing the scattered Ar^+ light from the card (while the filter F was moved away) using the method mentioned above. At this point, the intensity of the Ar^+ laser beam was reduced by the attenuator, and the transmitted fringes were observed on the monitor of the computer (DACS). The peaks were then made as narrow as possible by adjusting again the micrometer screws on the front plate. The three piezoelectric biases of the FP were adjusted to increase the finesse. Then the second laser beam was introduced by shutter ST, fibre FB and beam splitters BS1 and BS2. The position of the output end of the fibre was put at the focus of L3, and it was fine adjusted by observing the signal on the monitor (while shutter ST was open).

Finally, the cryostat was moved into the system again. Lens L4 was slightly adjusted to maximize the height of the Raman peak of liquid methane. The spectra of the samples could be recorded with the DACS in the drift-correction and finesse-correction modes.

4.6 Cryostat and Gas Handling System

Cooling was provided by a closed-cycle helium refrigerator (Air Products Model DE202).

We designed and built the tailsection of the cryostat and the gas handling system. The tailsection of the cryostat is shown in Figure 4.3. The outer body (4) was made of copper tube of 7 cm outer diameter which served as a vacuum shroud for the sample area. The copper outer radiation shield (3) was connected with the first-stage (~100K) heat sink (14) of the refrigerator. Both the outer wall and the outer radiative shield were highly polished to reduce radiative heat transfer as much as possible. The inner aluminum radiation shield (11) was maintained at the same temperature as the second-stage heat sink (13) of the refrigerator (about 5 to 6 K below the cell temperature). The quartz sample cell (8) was soldered to the dust collector assembly (24) using a quartz-to-kovar graded seal. The bottom of the cell was closed by a polished quartz plug. There were two clamps (6)(10) on the cell, each of them equipped with temperature sensitive diodes (9)(23) and heaters (7)(21). The copper cold head (16) was screwed to the top of the second-stage heat sink, with a heater (15) just beneath it . On the top of the cold head, there were the prism (19), the diode (18), and copper rods (12)(17). The prism reflected the laser light coming from the window on the other side of the tailsection (not shown in Figure 4.3) to the direction of the axis of the cell (Z direction). The diode (18) was used to measure the temperature of the cold head. Two copper rods (12)(17) served as the cold fingers. The copper braids (20) were

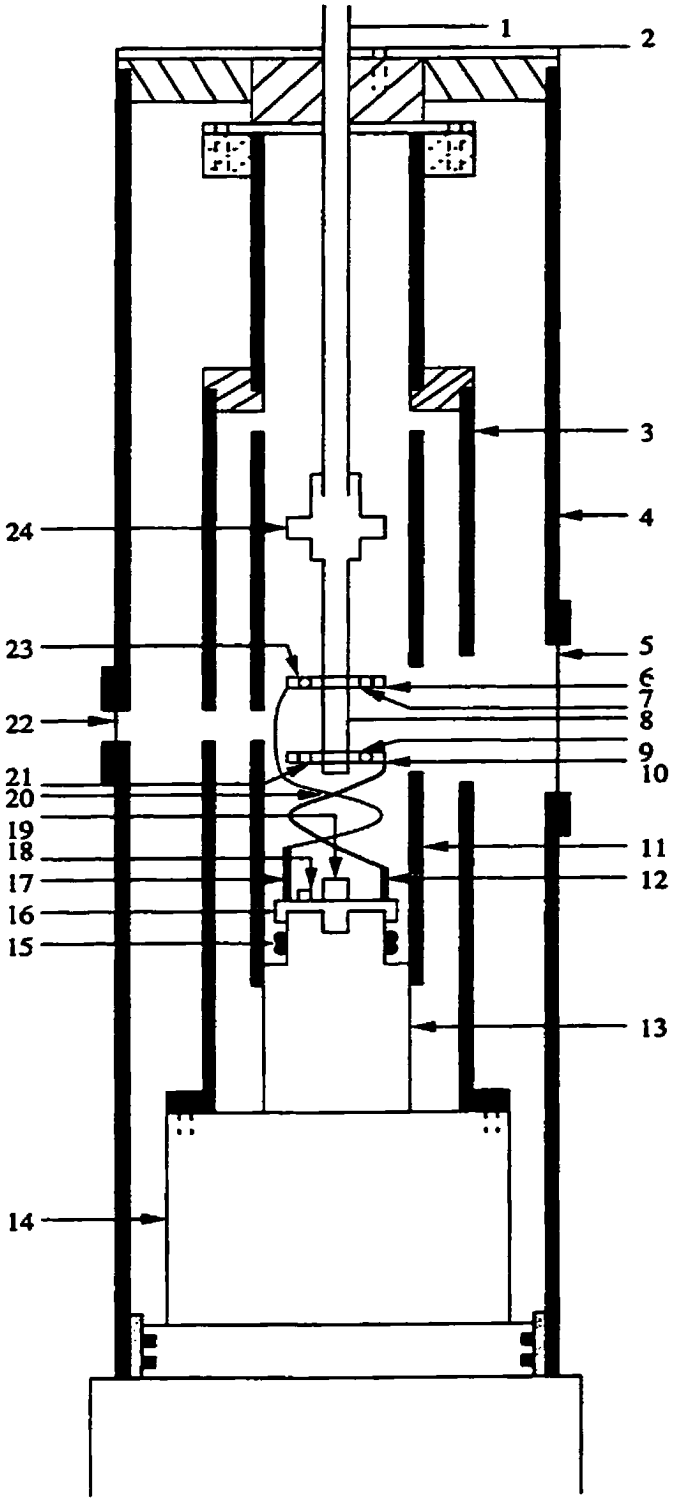

Figure 4.3: The Tail Section of the Cryostat

Figure 4.3: The Tailsection of The Cryostat

1 - Inlet Tube

2 - Rotary Assembly

3 - Ourter Radiation Shield

4 - Outer Wall

5 - Big Window

6 - Clamp

7 - Heater 1

8 - Cell

9 - Si Diode 2

10 - Clamp

11 - Inner Radiation Shield

12 - Copper Rod

13 - Second-Stage Heat Station of The Refrigerator

14 - First-Stage Heat Station of The Refrigerator

15 - Heater 3

16 - Cold Head

17 - Copper Rod

18 - Si Diode 3

19 - Prism

20 - Copper Braids

21 - Heater 2

soldered to these cold fingers. The top ends of the braids were soldered to the clamps (6)(10). The steel inlet tube (1) introduced the sample gas into the cell. Between the inlet tube and the sample cell, there was the dust collector assembly which had been described in detail in references [39, 40]. The dust collector assembly prevented dust particles from settling at the bottom of the cell. The inlet tube, the dust collector assembly and the sample cell were centred by means of teflon spacers. The cell could be rotated about the Z axis by the rotary assembly (2) with a scale to read the degree of rotation.

The scattered light was collected through the big window (5). Both the small window (20) and the big window (5) were made of plexiglass to allow the transmission of both X-rays and visible lights.

The cryostat was mounted on an aluminum table, and its position could be adjusted both along X and Y direction.

The gas handling system is shown in Figure 4.4. The methane gas used in the experiments was supplied by Matheson Co.. It was research grade with nominal purity of 99.99%.

The container of methane was connected to the inlet tube of the cryostat by copper tubes and a flexible stainless steel capillary tube. Four valves V1 to V4 were used to isolate the various parts of the gas handling system for evacuation or for filling the gas. The pressure gauge was used to monitor the pressure in the cell. Before the methane arrived at the inlet tube of the cryostat, it would pass through the filter (F).

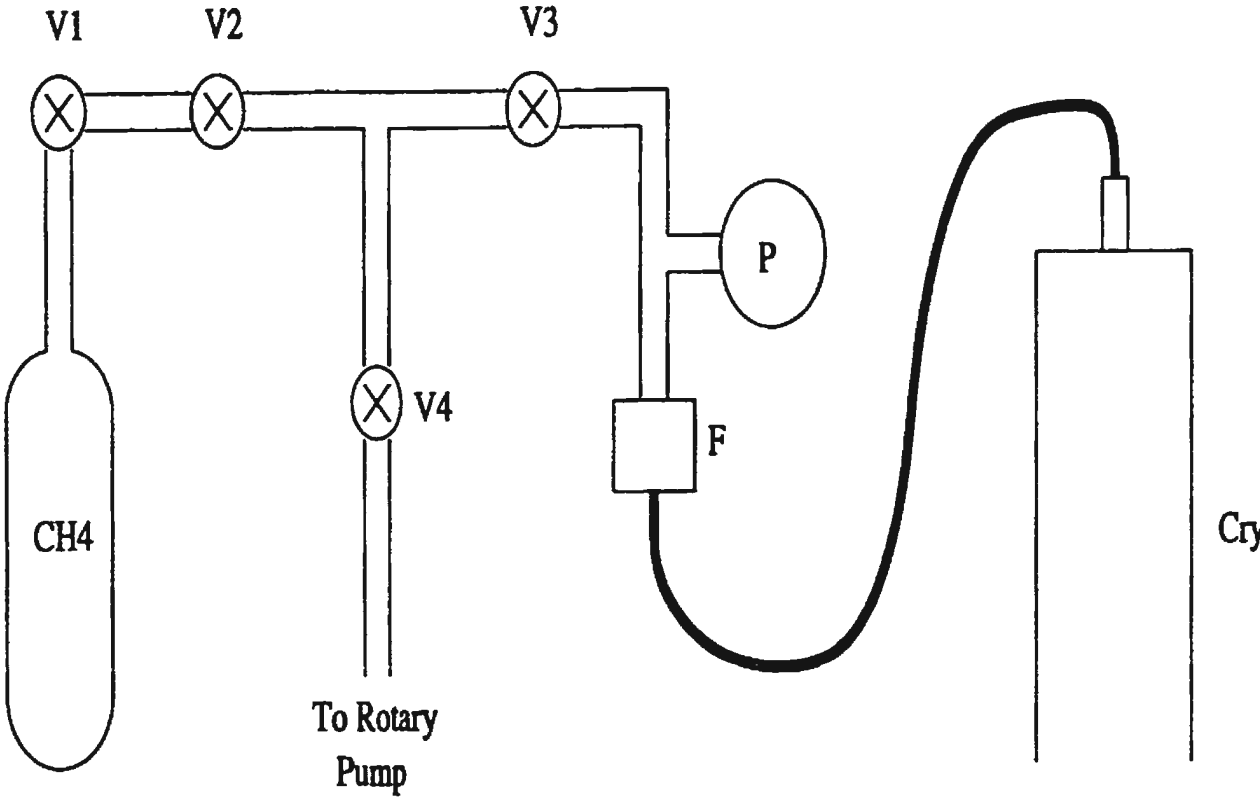

Figure 4.4: The Gas Handling System

4.7 Single-Crystal Growing

We first flushed the cell several times to remove possible gaseous impurities by using the methane gas and the pump, and then put the methane gas sample into the cell until the gas pressure reached about 700 torr.

The temperature of the cell was lowered to liquify the methane. The temperature of the liquid (at bottom of the cell) was kept at about 0.4 K above the triple point for about one day by the temperature control system which adjusted the currents to the heaters according to the feedback voltage from the diodes.

The crystals were grown by manually lowering the temperature of the cell at a rate about 0.2 K/hr until a small seed of about 0.05 mm was formed at the bottom of the cell. Then the temperature was further reduced manually to let the crystal to grow to about 8 mm at the rate of 1 mm/hr.

The quality of the crystal was checked by X-ray Laue diffraction photograph. Too many diffraction spots indicated that the crystal was probably polycrystalline. Strained crystals were easily recognized by the streaked nature or too many divisions of the spots. Strained or polycrystalline samples were melted completely and grown again.

When we took the Raman spectrum, the crystal was kept at a fixed temperature by the temperature control system. After finishing one spectrum,

we slowly reduced the temperature to another wanted value and measured the spectrum.

Chapter 5

Experimental Results and Discussion

5.1 Experimental Results

Methane gas of 99.99% purity (Matheson Co.) was used to grow the single crystals as explained in Section 4.7. The X-ray diffraction photographs were taken to ensure that the crystals were single and to determine their orientations.

Figure 5.1 shows the Laue diffraction picture of crystal #49 at 0^0 rotation of the cell. By using the computer programs ORT and LSORT in this laboratory, we got the Euler angles of this orientation to be $\theta = 59^0$, $\phi = 251^0$, $\chi = 252^0$. These Euler angles were consistent with the Euler angles obtained at -15^0 and -20^0 rotation of the cell. The uncertainty of the Euler angles was within $\pm 1^0$.

Figure 5.2 (a) and (b) show the parallel (depolarized) and perpendicular (polarized) components of the Raman spectrum of crystal #49 at 89.4 K

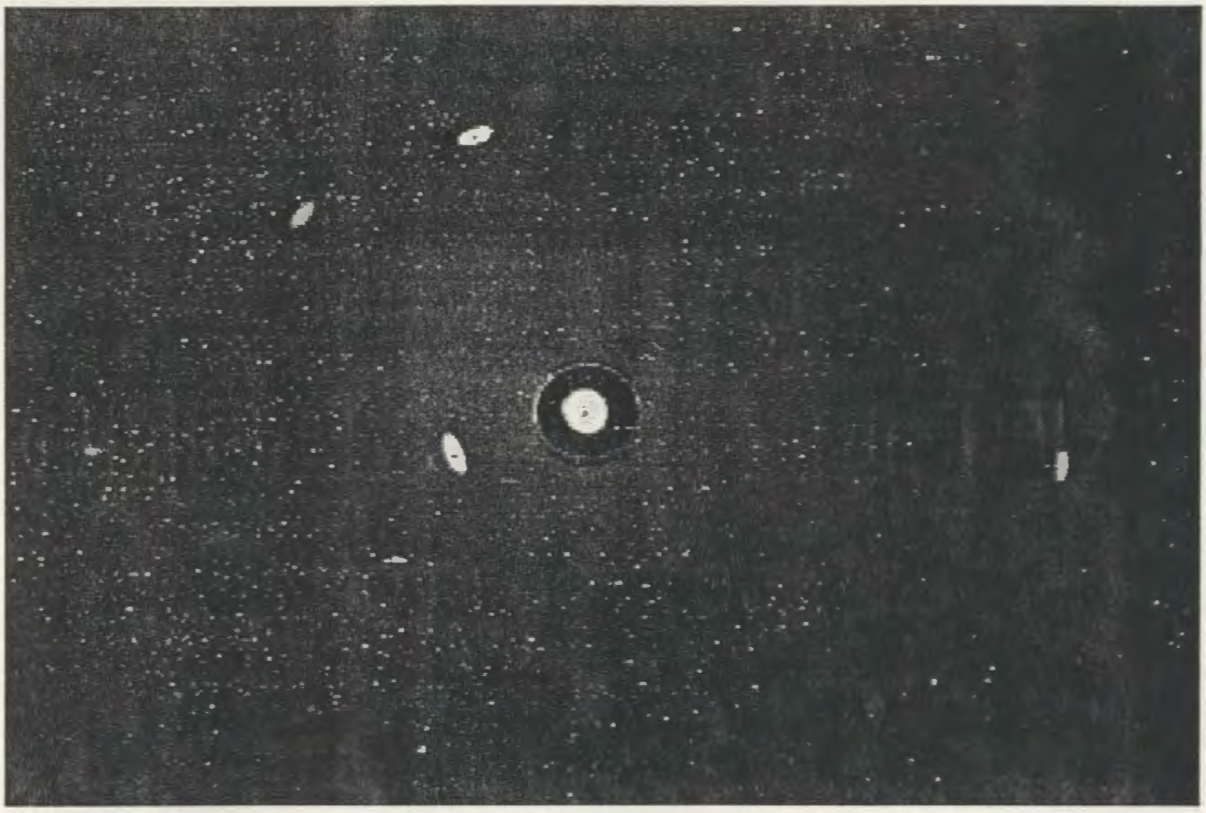

Figure 5.1: X-Ray Diffraction Picture of Crystal #49

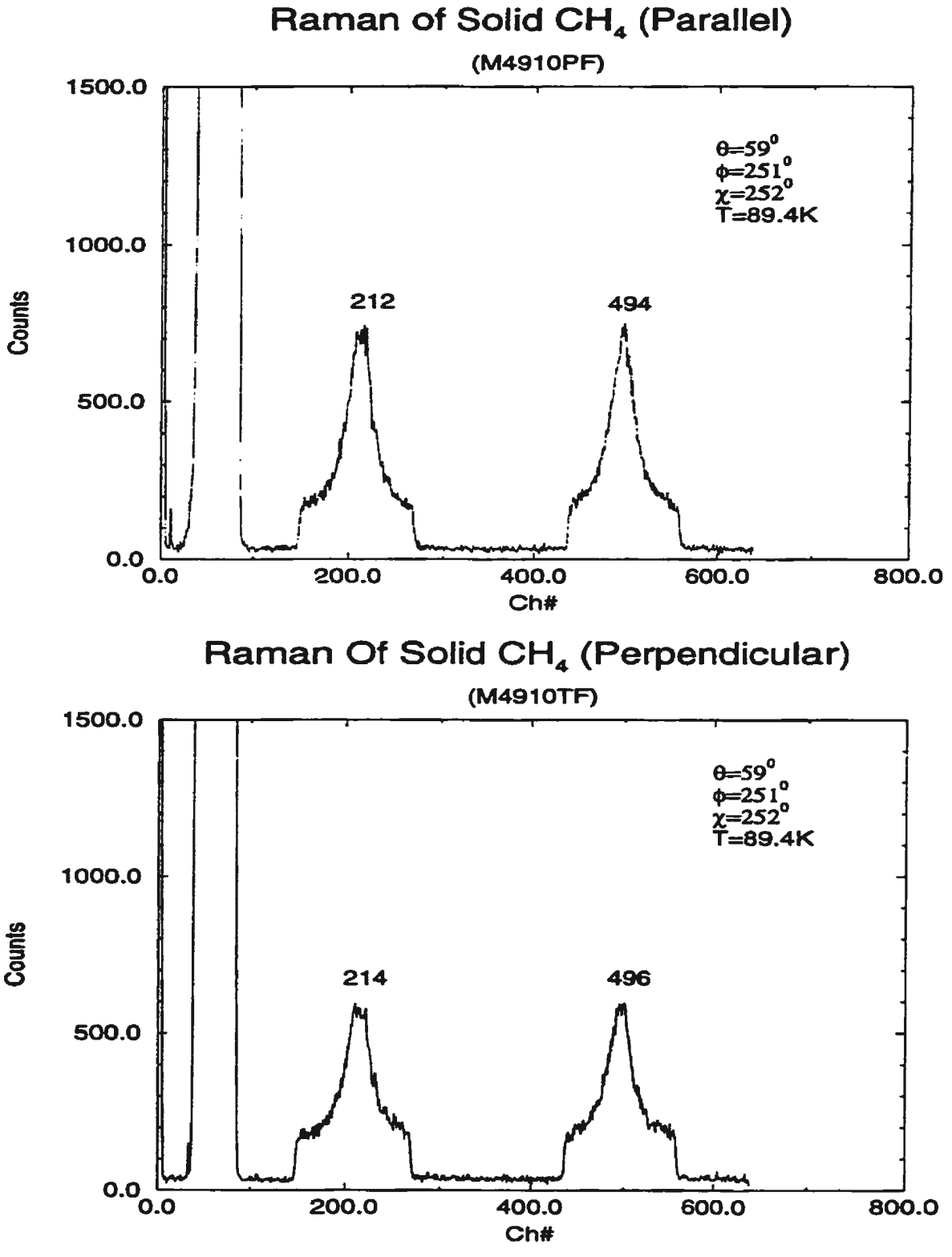

Figure 5.2: Raman Spectra of Solid CH_4 (#49). (a) Parallel (b) Perpendicular

and 0^0 rotation of the cell. There are two orders of Raman peaks at channel number 212 (214) and 494 (497). The strong peak at channel number 60 is the reference laser line coming from the shutter (ST) and the fibre (FB).

The experimental results of crystal #49 at different orientations and different temperature are listed in Table 5.1. The uncertainties for the difference of the frequencies (channel number) and the width (Γ') are ± 1 and ± 2 channel respectively. The depolarization ratios (ρ) were calculated from the ratios of the areas under the corresponding Raman peaks (after cutting the background). The relative uncertainties for the depolarization ratios are 5% at high temperature (89.4 K) and 9% at low temperature (21.8 K).

The experimental results of crystal #28 and #36 are listed in the Table 5.2 and 5.3.

Table 5.1: The Experimental Results of Crystal #49 ($\theta = 59^0$, $\chi = 252^0$)

$T(K)$	ϕ	$f_{\parallel} - f_r(ch)$	$f_{\perp} - f_r(ch)$	$\Gamma'_{\parallel}(ch)$	$\Gamma'_{\perp}(ch)$	ρ	S_1	S_2
	236^0	155	154	22	23	1.34		
	241^0	157	153	24	24	1.52		
89.4	251^0	152	154	23	24	1.65	14	4.0
	261^0	156	156	24	24	1.64		
	266^0	157	157	23	25	1.60		
	236^0	161	158	25	25	1.17		
	241^0	160	161	23	24	1.18		
79.7	251^0	158	156	23	23	1.10	19	19
	261^0	162	162	26	25	1.07		
	266^0	155	159	23	24	1.31		
	236^0	158	156	22	22	0.900		
	241^0	155	154	23	22	1.04		
69.2	251^0	156	156	23	19	0.779	11	13
	261^0	157	152	21	21	0.894		
	266^0	154	157	22	22	0.976		
	236^0	160	162	22	21	0.755		
	241^0	159	160	21	22	0.891		
59.2	251^0	159	161	18	21	0.974	8.5	5.8
	261^0	148	155	24	22	0.926		
	266^0	151	151	27	24	0.900		
	236^0	169	168	23	21	0.815		
	241^0	164	168	20	21	0.995		
49.4	251^0	164	164	21	21	1.02	10	6.4
	261^0	170	163	23	21	1.02		
	266^0	160	154	21	22	0.956		
	236^0	164	172	20	23	0.461		
	241^0	162	166	18	20	0.402		
27.9	251^0	165	166	19	19	0.537	5.2	2.0
	261^0	159	159	20	21	0.592		
	266^0	162	165	22	20	0.841		
26.0	251^0	166	166	19	19	0.508		
23.0	251^0	166	167	21	20	0.474		
21.8	251^0	176	176	17	20	0.372		
23.0	251^0	168	169	17	20	0.352		
25.0	251^0	169	171	21	21	0.321		

Table 5.2: The Experimental Results of Crystal #28 ($\theta = 74^0$, $\phi = 252^0$ $\chi = 340^0$)

$T(K)$	$f_{\parallel} - f_r$ (ch)	$f_{\perp} - f_r$ (ch)	$\Gamma'_{\parallel}$ (ch)	$\Gamma'_{\perp}$ (ch)	ρ
87.2	186	189	28	25	1.57
77.8	193	194	23	24	0.822
65.6	197	198	24	25	0.617
55.3	197	198	25	23	0.622
43.3	201	201	19	22	0.450
33.2	201	204	19	23	0.454
27.1	209	208	24	24	0.418
24.3	205	207	18	22	0.258

Table 5.3: The Experimental Results of Crystal #36 ($\theta = 73^0$, $\phi = 102^0$, $\chi = 346^0$)

$T(K)$	$f_{\parallel} - f_r$ (ch)	$f_{\perp} - f_r$ (ch)	$\Gamma'_{\parallel}$ (ch)	$\Gamma'_{\perp}$ (ch)	ρ
61.7	199	201	24	26	0.534
58.9	220	220	32	23	0.921
42.0	221	220	20	18	0.558
28.6	220	223	31	22	0.407
26.8	218	221	29	22	0.420

5.2 The Depolarization Ratios

From Table 5.1, 5.2 and 5.3, we can see that the depolarization ratios for the CH_4 crystals are not zero, and they change with the temperature.

Figures 5.3, 5.4, 5.5 and 5.6 show the temperature dependence of the depolarization ratios for crystal #49, #28 and #36. From these graphs, we can see that at high temperature (89.4 K, 87.2 K), the values of the depolarization ratios, ρ, are high ($\sim$ 1.5). When the temperature decreases, the values of ρ first decrease rapidly, then increase a small amount and form a local maximum at the temperature range between 45 K and 60 K. After that maximum point, the values of ρ decrease again.

Rose, Whitewolf, and Baglin measured the density (pressure) dependence of the depolarization ratio, ρ, and the frequency for ν_1 mode in high pressure CH_4 gas [42]. Their results are illustrated in Figure 5.7.

We took the Raman spectra for the gaseous CH_4 sample at 750 τ ($16^0C, \sim 110mW$) and only got the spectrum for the polarized (perpendicular) component. The depolarized (parallel) component was too small to be detected ($\sim$ 18 hr). This result meant that the depolarization ratio was almost zero in the CH_4 gas sample at 750 τ. This was consistent with Rose's result.

Our depolarization ratio results in the crystals were about one order higher than Rose's results in the high pressure gas. From Section 3.3, we can see that for substance in which molecular orientation is perfectly random, the maximum values of the Raman depolarization ratios are $\frac{6}{7}$, $\frac{3}{4}$ and

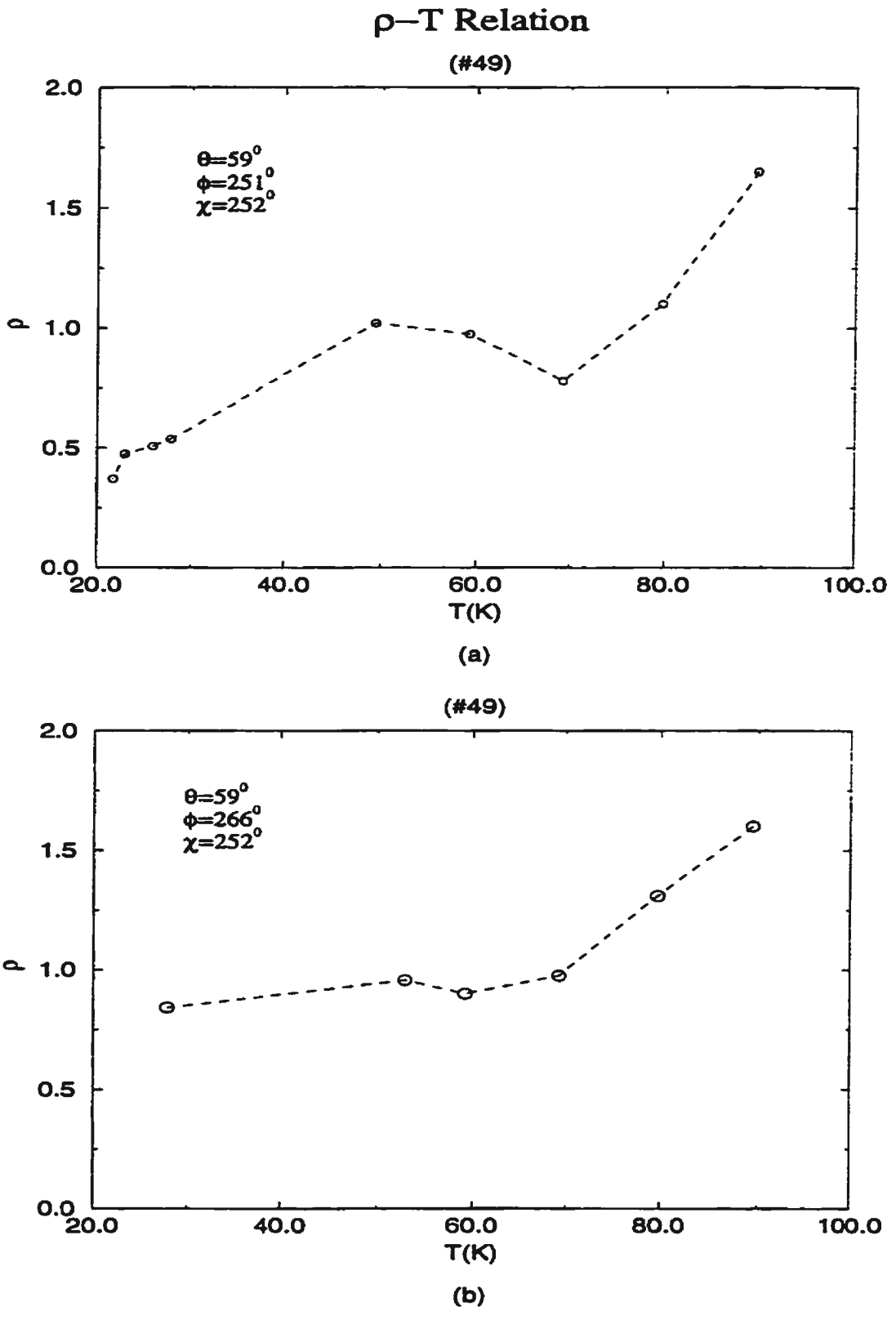

Figure 5.3: ρ-T Relation (#49)

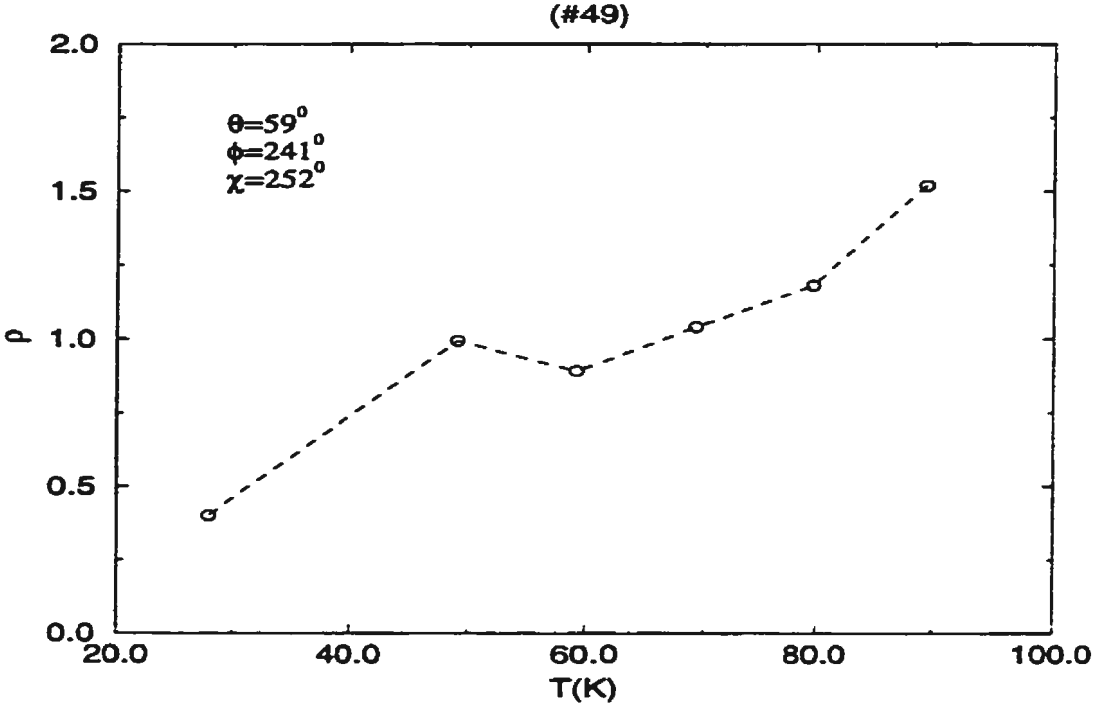

Figure 5.4: ρ-T Relation (#49)

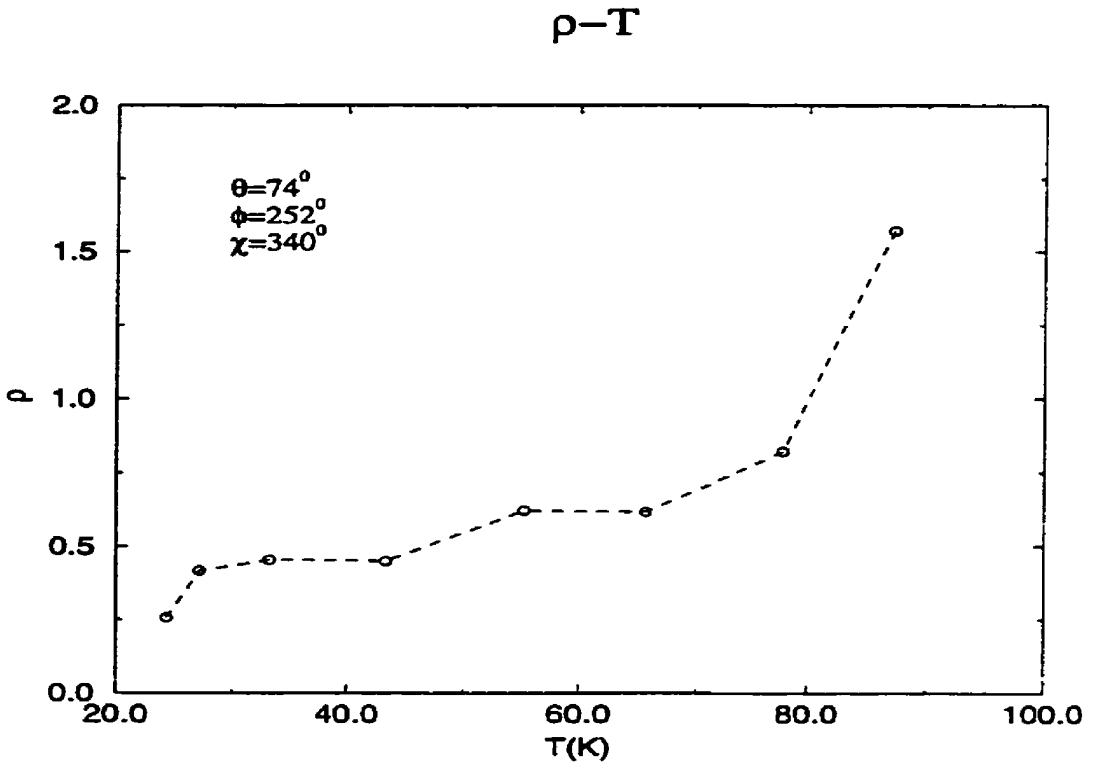

Figure 5.5: ρ-T Relation (#28)

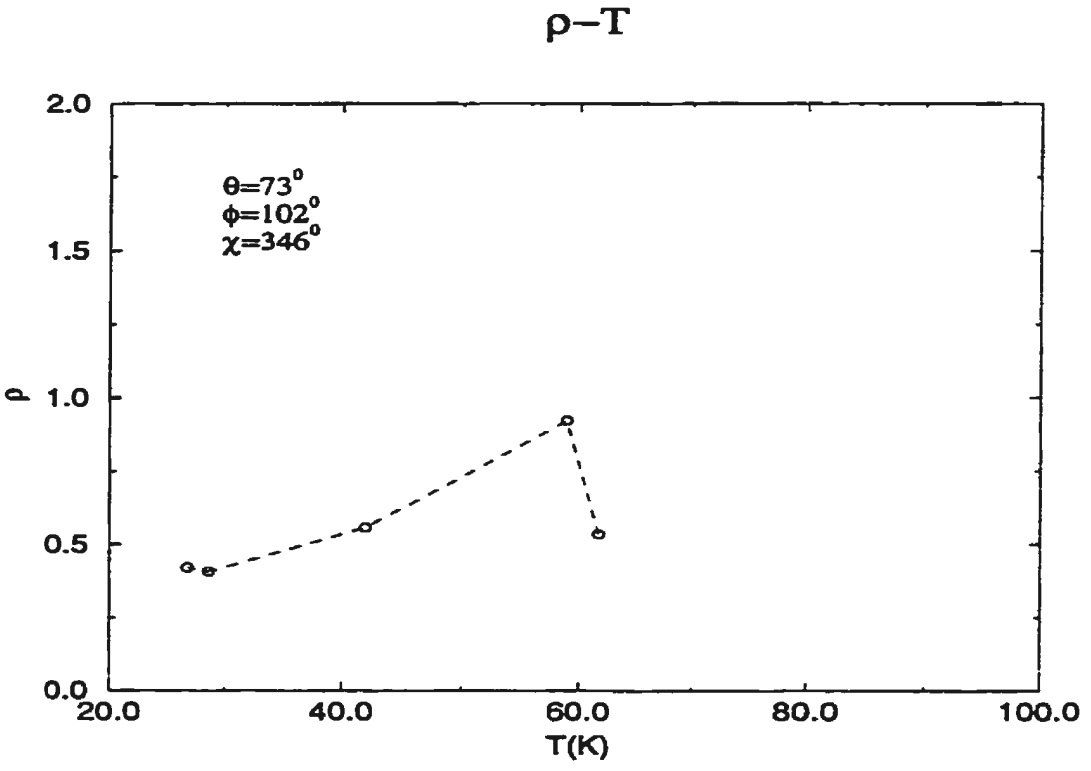

Figure 5.6: ρ-T Relation (#36)

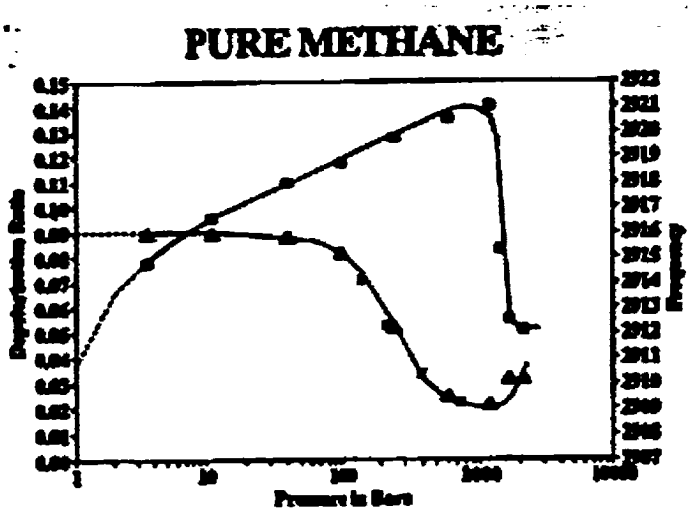

Figure 5.7: Pure methane depolarization ratio (boxes) and frequency values of ν_1 (band center) as a function of pressure (triangles).

1 for natural, linearly and elliptically polarized incident light, respectively. Our depolarization ratio results at high temperature (just below the triple point) were larger than 1. This indicated the molecular orientations in the high temperature crystal samples were not perfectly random (May be there were some preferred orientations.).

Press [26] detected an indication of partial order in phase I of CD_4 at 77 K in the neutron scattering experiment, and this indication disappeared at 35 K. Similar things possibly happened in solid CH_4 in our experiments.

Rose and the co-workers explained the nonzero depolarization ratios on the basis of the pentad interaction [42, 43]. The pentad diagram is shown in Figure 5.8.

In Figure 5.8, the purely vibrational interactions (between same species) are indicated by solid lines, Coriolis-type interactions (between different species) by dashed lines. From Figure 5.8, we can see that the totally symmetric stretching mode of the CH_4 molecular system is involved in a very complicated vibrational and rotational resonance pattern comprising ν_1, $2\nu_2$, $2\nu_4$, ν_3 and $\nu_2 + \nu_4$, These resonances effectively mix the A_1, E, F_2 and F_1 states. Therefore the depolarization ratio in this frequency range is not zero.

In Table 3.4, we listed the depolarization ratios of T_d type molecule for six different partial orientations. From these results we can see that if the orientations of molecules are not random, the combination of the A_1, E, F_2 and F_1 states could result in a value of ρ that is large than 1.

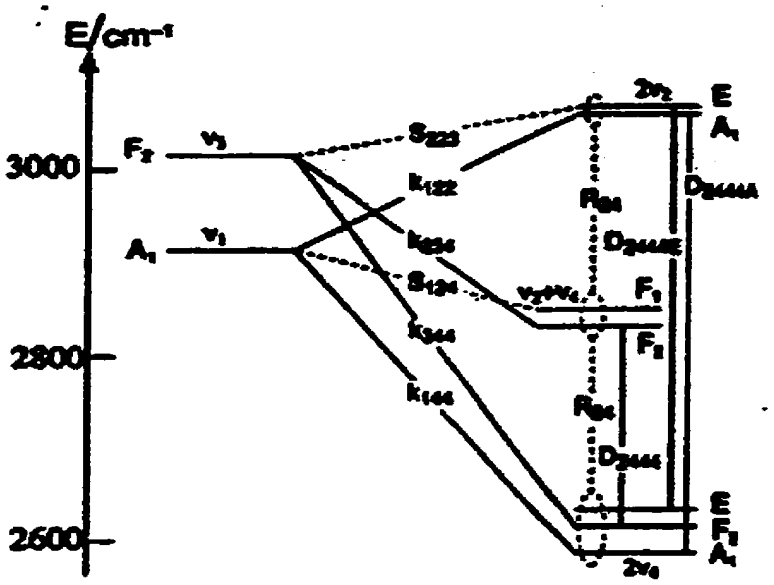

Figure 5.8: Pentad diagram shows that the J=0 upper state levels of the ν_1, ν_3, $2\nu_2$, $\nu_2 + \nu_4$ bands in CH_4 levels are labeled by their T_d symmetry species.

When the temperature decreases, there are three factors which can affect the depolarization ratio ρ: (1) The density increases, therefore the fluctuations of the intramolecular forces will increase. This will increase the distortion and make ρ larger. (2) The rotation (ω) decreases, the vibration-rotation coupling (Coriolis-type) also decrease. This will make the ν_1 mode close to A_1 type (the mixing decrease), and make the ρ smaller. (3) The orientations of the molecules might change, and therefore influence ρ. These factors result in the complex relationship between ρ and T in Figure 5.3, 5.4, 5.5 and 5.6.

For some arrangements of molecular orientations, for example, the orientation arrangement of phase II of CH_4 crystal, the depolarization ratios will be small for some crystal orientation.

The crystal structure of phase II is shown in Figure 2.4. There are eight molecules per primitive cell. The orientations of molecules 1 and 2 are random. Molecules 3 to 8 are orientationally ordered. Their rotation matrices can be written as

$$R_3 = \begin{pmatrix} 1 & 0 & 0 \\ 0 & K & -K \\ 0 & K & K \end{pmatrix}, \quad R_4 = \begin{pmatrix} -1 & 0 & 0 \\ 0 & -K & K \\ 0 & K & K \end{pmatrix}$$

$$R_5 = \begin{pmatrix} 0 & K & -K \\ -1 & 0 & 0 \\ 0 & K & K \end{pmatrix}, \quad R_6 = \begin{pmatrix} 0 & -K & K \\ 1 & 0 & 0 \\ 0 & K & K \end{pmatrix}$$

$$R_7 = \begin{pmatrix} -K & -K & 0 \\ K & -K & 0 \\ 0 & 0 & 1 \end{pmatrix}, \quad R_8 = \begin{pmatrix} K & -K & 0 \\ K & K & 0 \\ 0 & 0 & 1 \end{pmatrix} \qquad (5.1)$$

where

$$K = \frac{\sqrt{2}}{2}$$

The contribution of molecules 3,4,...,8 to the polarizability derivative can be written as (in crystal coordinates)

$$\alpha'_{3-8} = \sum_{i=3}^{8} R_i \alpha'_i R_i^{-1} \tag{5.2}$$

The results for different species are listed in Table 5.4. In the last two columns of the Table 5.4, we listed the components of $\overline{\alpha'^2_{(1-8),XX}}$ and $\overline{\alpha'^2_{(1-8),XZ}}$ (in laboratory system XYZ), which are the contributions from one primitive cell (phase II).

From Table 5.4, we can see that:

(a) For all species listed in Table 5.4, the maximum values of $\overline{\alpha'^2_{(1-8),XX}}$ and $\overline{\alpha'^2_{(1-8),XZ}}$ for phase II are smaller than the corresponding values for the case where all molecules have the same orientation.

(b) For F_{2c} species, the values of $\overline{\alpha'^2_{(1-8),XX}}$ and $\overline{\alpha'^2_{(1-8),XZ}}$ for phase II are less than the values for random case.

(c) For some crystal orientations, the values of $\overline{\alpha'^2_{(1-8),XX}}$ and $\overline{\alpha'^2_{(1-8),XZ}}$ for phase II are smaller than the corresponding values for random case.

Table 5.4: The Contributions of 8 Molecules to $\overline{\alpha'^2_{(1-8),XX}}$ and $\overline{\alpha'^2_{(1-8),XZ}}$

Species	*Orientation*	α'_{3-8}	$\overline{\alpha'^2_{(1-8),XX}}$	$\overline{\alpha'^2_{(1-8),XZ}}$
F_{2a}	Phase II	$c\begin{pmatrix} -2 & 0 & -\sqrt{2} \\ 0 & -2 & 0 \\ -\sqrt{2} & 0 & 4 \end{pmatrix}$	$4c^2(2R_{13}^2 - R_{12}^2 - R_{11}^2 - \sqrt{2}R_{11}R_{13})^2 + \frac{7}{16}c^2$	$c^2(4R_{13}R_{33} - \sqrt{2}R_{13}R_{31} - 2R_{11}R_{33} - \sqrt{2}R_{11}R_{31})^2 + \frac{1}{1}$
	Random		$\frac{7}{4}c^2$	$\frac{21}{16}c^2$
	Same Orientation	$6c\begin{pmatrix} 0 & 0 & 0 \\ 0 & 0 & 1 \\ 0 & 1 & 0 \end{pmatrix}$	$64\times4c^2R_{12}^2R_{13}^2$	$64c^2(R_{12}R_{33} + R_{13}R_{32})$
F_{2b}	Phase II	$\sqrt{2}c\begin{pmatrix} 0 & 0 & 0 \\ 0 & 0 & 1 \\ 0 & 1 & 0 \end{pmatrix}$	$8c^2R_{12}^2R_{13}^2 + \frac{7}{16}c^2$	$2c^2(R_{12}R_{33} + R_{13}R_{32})^2 + \frac{21}{64}c^2$
	Random		$\frac{7}{4}c^2$	$\frac{21}{16}c^2$
	Same Orientation	$6c\begin{pmatrix} 0 & 0 & 1 \\ 0 & 0 & 0 \\ 1 & 0 & 0 \end{pmatrix}$	$64\times4c^2R_{11}^2R_{13}^2$	$64c^2(R_{11}R_{33} + R_{13}R_{31})$
F_{2c}	Phase II	$\begin{pmatrix} 0 & 0 & 0 \\ 0 & 0 & 0 \\ 0 & 0 & 0 \end{pmatrix}$	$\frac{5}{12}c^2$	$\frac{5}{16}c^2$
	Random		$\frac{5}{3}c^2$	$\frac{5}{4}c^2$
	Same Orientation	$6c\begin{pmatrix} 0 & 1 & 0 \\ 1 & 0 & 0 \\ 0 & 0 & 0 \end{pmatrix}$	$64\times4c^2R_{11}^2R_{12}^2$	$64c^2(R_{11}R_{32} + R_{12}R_{31})$
E_b	Phase II	$\sqrt{3}b\begin{pmatrix} -1 & 0 & 0 \\ 0 & -1 & 0 \\ 0 & 0 & 2 \end{pmatrix}$	$((3R_{13}^2 - 1)^2 + \frac{5}{12})3b^2$	$(9R_{13}^2R_{33}^2 + \frac{5}{16})3b^2$
	Random		$5b^2$	$\frac{15}{4}b^2$
	Same Orientation	$6\sqrt{3}b\begin{pmatrix} -1 & 0 & 0 \\ 0 & 1 & 0 \\ 0 & 0 & 0 \end{pmatrix}$	$64\times3b^2(R_{12}^2 - R_{11}^2)^2$	$64\times3b^2(R_{12}R_{32} - R_{11}R_{31}$
E_a	Phase II	$3\ b\begin{pmatrix} 1 & 0 & 0 \\ 0 & 1 & 0 \\ 0 & 0 & -2 \end{pmatrix}$	$(3(1\text{-}3R_{13}^2)^2 + \frac{1}{2})3b^2$	$(9R_{13}^2R_{33}^2 + \frac{1}{8})9b^2$
	Random		$6b^2$	$\frac{9}{2}b^2$
	Same Orientation	$6b\begin{pmatrix} 1 & 0 & 0 \\ 0 & 1 & 0 \\ 0 & 0 & -2 \end{pmatrix}$	$64b^2(1 - 3R_{13}^2)^2$	$64\times9b^2R_{13}^2R_{33}^2$

Table 5.5: Depolarization Ratios For Different types of Vibrations. ($F_1 = 48 \times 9R_{13}^2R_{33}^2$, $F_2 = 48(3R_{13}^2-1)^2$, $F_3 = 64(4R_{13}R_{33}-\sqrt{2}R_{13}R_{31}-2R_{12}R_{32}-\sqrt{2}R_{11}R_{33}-2R_{11}R_{31})^2$, $F_4 = 16^2(2R_{13}^2-R_{12}^2-R_{11}^2-\sqrt{2}R_{11}R_{13})^2$, $F_5 = 128(R_{12}R_{33}+R_{13}R_{32})^2$, $F_6 = 64 \times 8R_{12}^2R_{13}^2$)

Orientation	*Phase II*					
Species	A_1	E_a	E_b	F_{2a}	F_{2b}	F_{2c}
ρ	0	$\frac{F_1+6}{F_2+8} \neq \infty$	$\frac{F_1+15}{F_2+20} \neq \infty$	$\frac{F_3+21}{F_4+28} \neq \infty$	$\frac{F_5+21}{F_6+28} \neq \infty$	$\frac{3}{4}$
Orientation	*Random*					
Species	A_1	E_a	E_b	F_{2a}	F_{2b}	F_{2c}
ρ	0	$\frac{3}{4}$	$\frac{3}{4}$	$\frac{3}{4}$	$\frac{3}{4}$	$\frac{3}{4}$

In our experiments, we found that the intensity I_{XZ}, I_{XX} at 89 K were about 10 times the values at 21.8 K. This was possibly a sign of orientation change.

Table 5.5 listed the theoretical depolarization ratio, ρ, for different types of vibrations. Comparing this table with Table 3.4, we can see that the depolarization ratios of phase II for F_{2a}, F_{2b} and F_{2c} species are smaller than the values for some partial orientation cases. For certain combinations of the species, ρ of phase II is smaller than some partial orientation cases.

The angular dependence of the depolarization ratios for crystal #49 is shown in Figure 5.9, where the experimental results corresponding to different temperatures are indicated by circles, triangles, diamonds, squares,... From Figure 5.9, we can see that for the same temperature, the depolarization ratio, ρ, changes with angle ϕ.

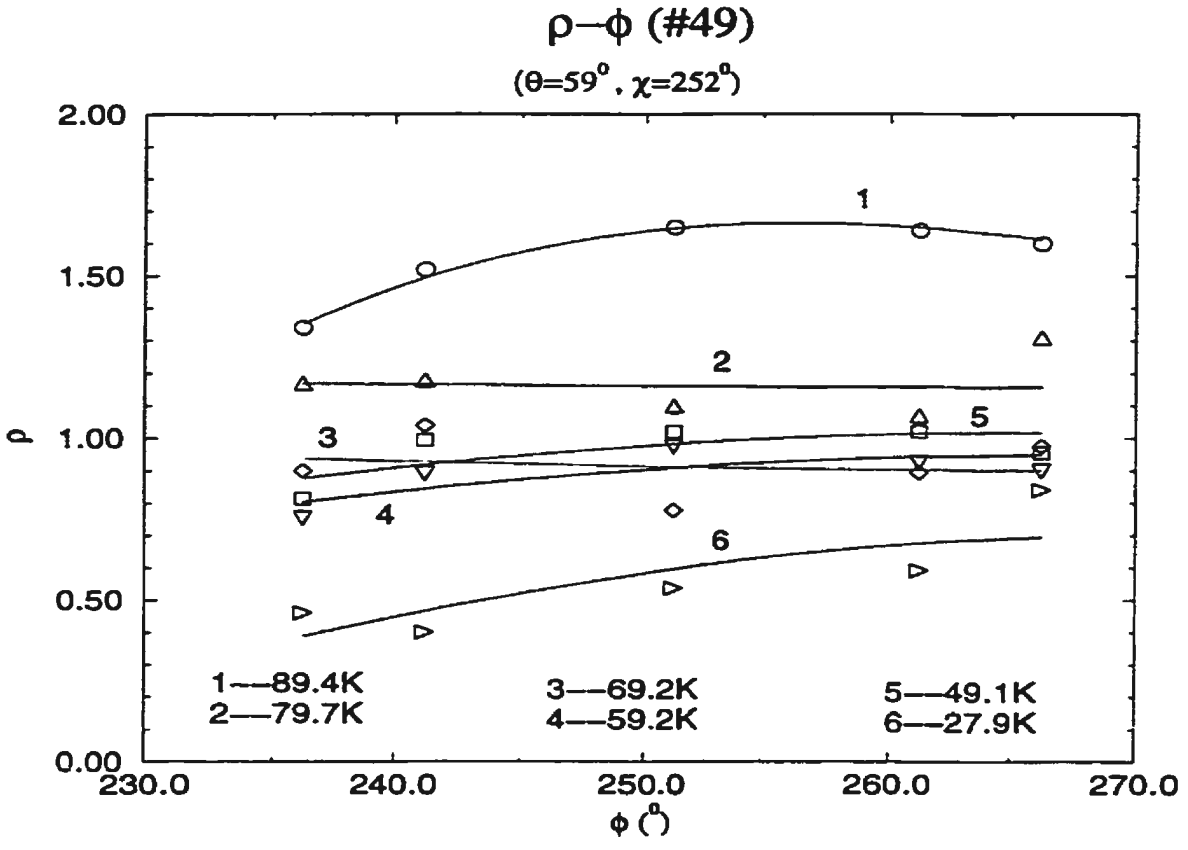

Figure 5.9: The Angular Dependency of ρ (#49)

We used equation 3.17 to do the fitting, the results were indicated by solid lines in Figure 5.9. The fitting parameters $S_1(a_{22}/a_{11})$ and $S_2(a_{33}/a_{11})$ are listed in the last two columns of Table 5.1.

The fittings are good for some temperatures, for example 89.4 K (1), but not good for some other temperatures, for example 69.2 K (3). These indicate that the assumption for equation 3.17 is not valid. The principal axes are not along the C_4 axes of the crystal. We need to use equation 3.14 to do the fitting (five parameters), which requires more experimental data.

5.3 Frequency and Width

Figures 5.10, 5.11, 5.12 and 5.13 show the temperature dependency of frequencies of crystal #49, #28 and #36. From these graphs, we can see when the temperature changes, the frequencies will have complex changes.

Cabana and Thé [27] observed that the frequency of ν_1 for phase II at 9 K was 3.3 cm^{-1} smaller than that for phase I (just above the transition temperature). Anderson and Savoie [29] found that the ν_1 frequency for phase II at 12 K was 4 cm^{-1} lower than that for phase I at 77 K. In our experiments, the measured frequency at 21.8 K is 2.5 cm^{-1} (24 channel) higher than that at 89.4 K. The measured frequency (ν_o) was the difference between the laser frequency (ν_L) and the Raman frequency (ν_1) ($\nu_o = \nu_L - \nu_1$). Therefore the Raman frequency of ν_1 at 21.8 K is 2.5 cm^{-1} lower than that at 89.4 K. this is consistent with their results.

Comparing Figures 5.10 - 5.13, with Figures 5.3-5.6, we can find that the temperature dependence of the frequency is correlated to the temperature dependence of the depolarization ratio. At the temperature near the point of local maximum of ρ, there will be a shallow maximum of measured frequency. This is consistent with Rose's results in the high density gas [42].

When temperature decreased, the frequency changes were caused by several sources : (1) The volume of the crystal would decrease. According to pseudo-harmonicity theory [33], this would move ν_1 (shift) to higher frequencies. The measured frequency (absolute) would decrease. (2) The anharmonic terms (phonon coupling) would shift ν_1 to lower frequencies (usually

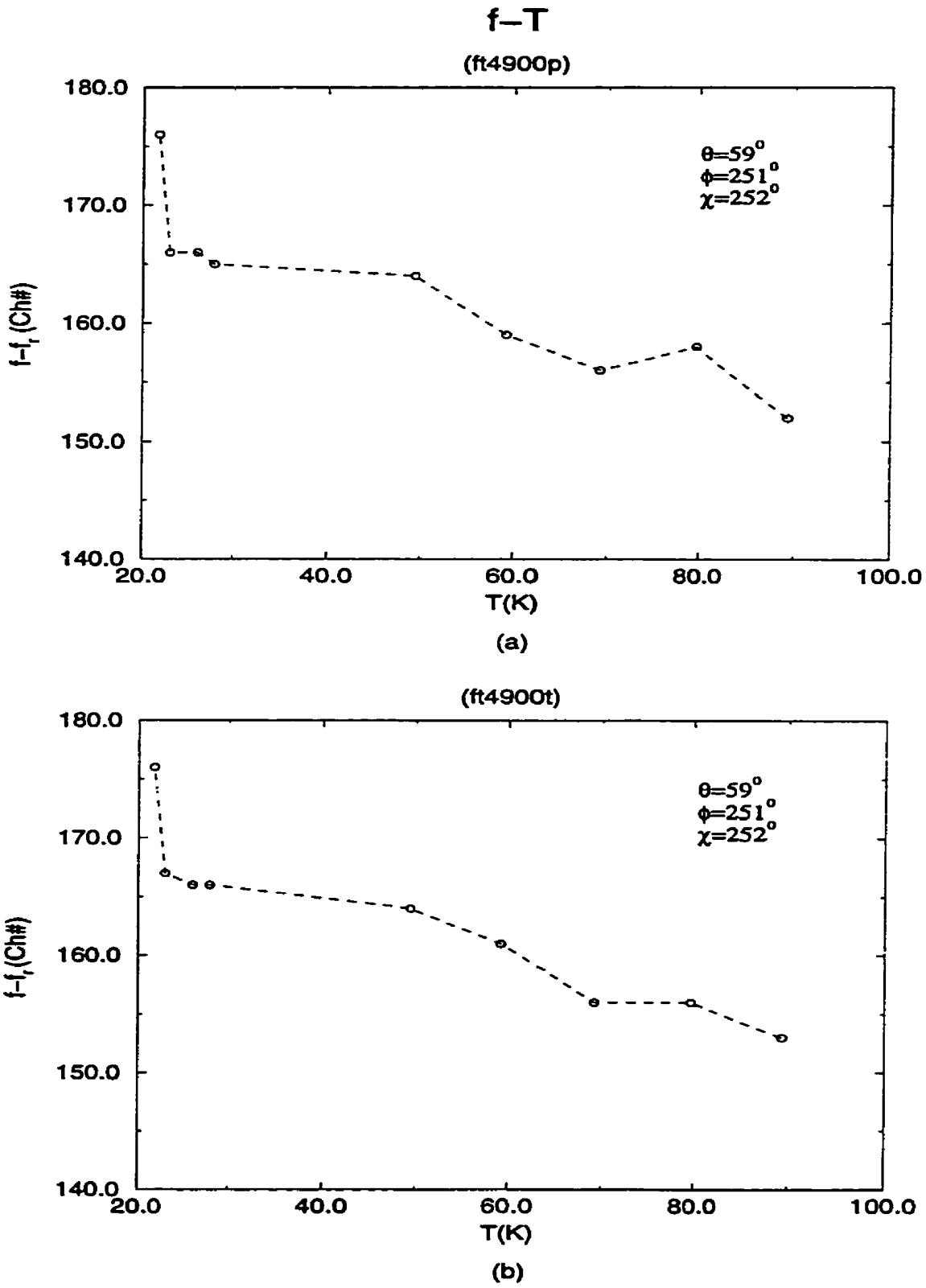

Figure 5.10: f-T Relation of Crystal #49 at $\phi = 251^0$. (a) Parallel (b) Perpendicular

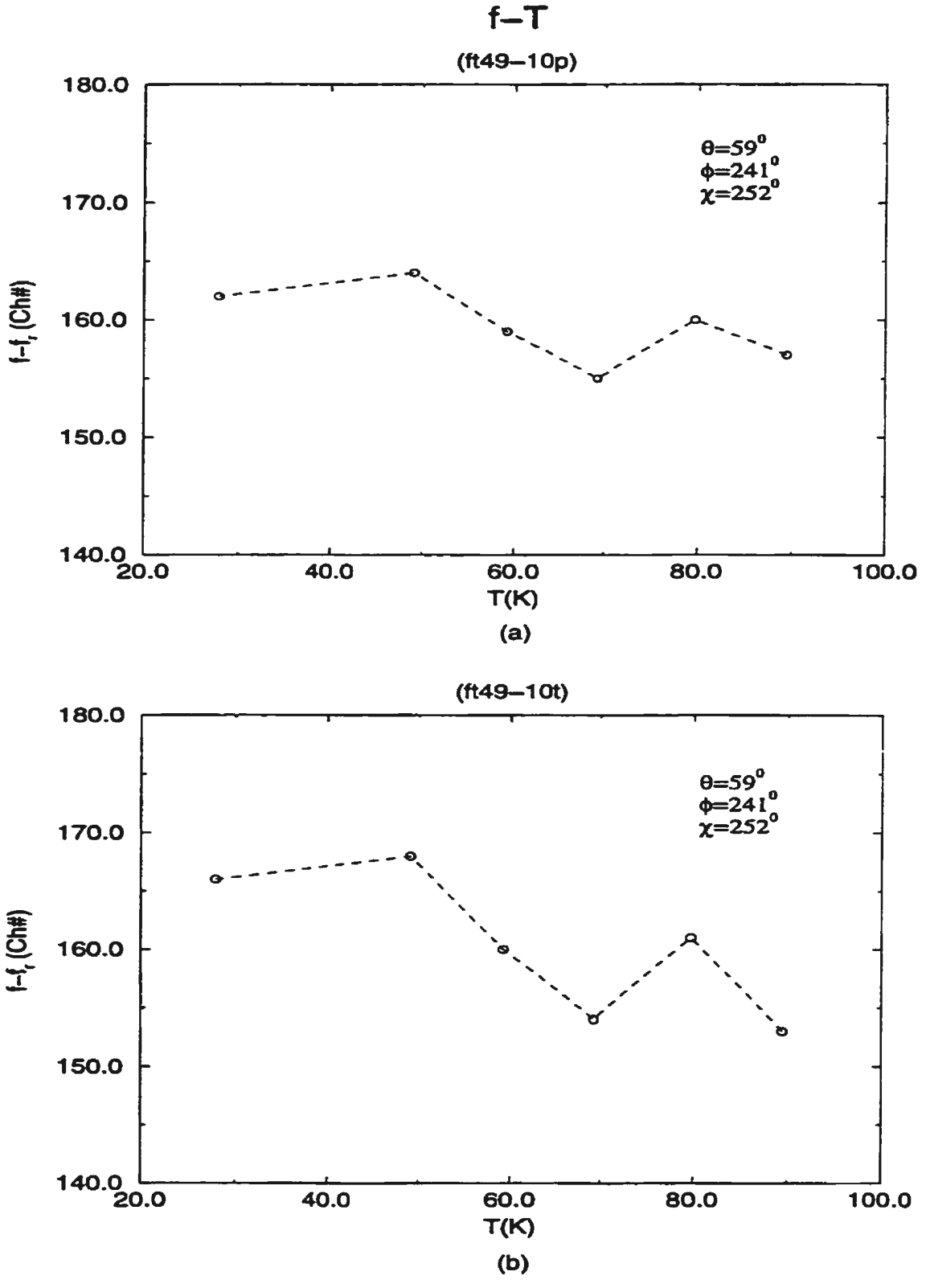

Figure 5.11: f-T Relation of Crystal #49 at $\phi = 241^0$. (a) Parallel (b) Perpendicular

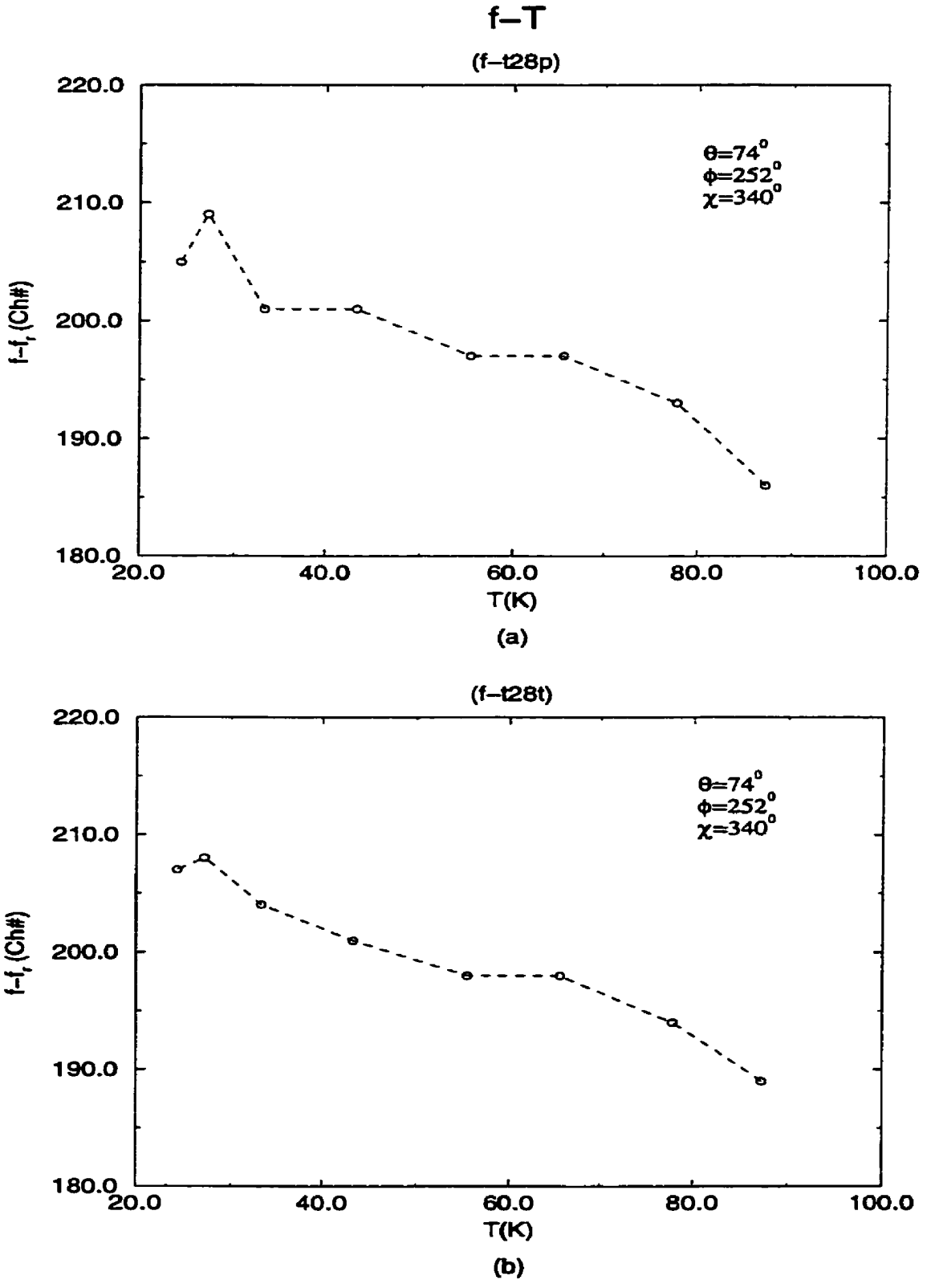

Figure 5.12: f-T Relation of Crystal #28. (a) Parallel (b) Perpendicular

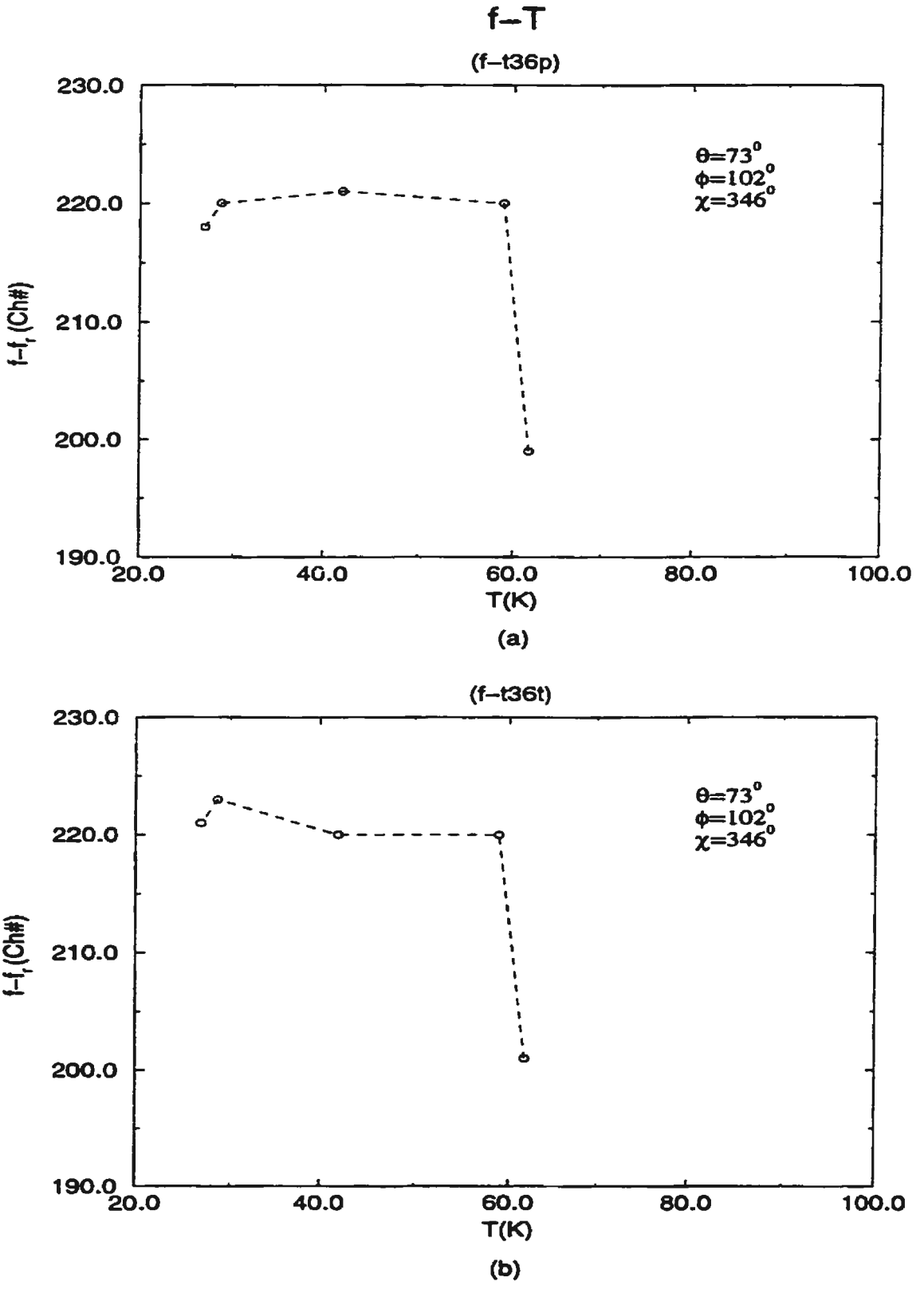

Figure 5.13: f-T Relation of Crystal #36. (a) Parallel (b) Perpendicular

this kind shift was smaller than 'pseudo-harmonicity shift' [42].). (3) The rotations decrease, and make vibration-rotation coupling smaller. This would influence the frequency ν_1. (4) The molecular orientation changes and therefore changes the frequency ν_1. According to references [26, 27, 29], the phase change from phase I to phase II is due to the orientation change. This kind of orientation change makes ν_1 shift to lower frequency. In our experiments, the measured frequency varied rapidly with the temperature near 21.8 K (the magnitude of the slope was very big.). This might indicate the beginning of the phase transition (orientation change).

The orientation dependence of the frequency for crystal #49 at 89.4 K is shown in Figure 5.14 (a) and (b). From these graphs we can see that for same temperature, the frequency (ν_1) changes with angle (ϕ_1). The range of the change is about 5 channels ($\sim 16GHz$). This may be indicates that the interaction potential energy (perturbation) is orientation dependent in the crystal.

The orientational dependence of depolarized (perpendicular) component is different from that of polarized (perpendicular) component. This is because they have different origins. The polarized component comes from the contributions of both the totally symmetric species A_1 and other unsymmetric species. But A_1 doesn't contribute to the depolarized component.

Figures 5.15, 5.16 and 5.17 show the temperature dependence of the width (FWHM) for crystals #49, #28 and #36, respectively. Comparing these graphs with the corresponding temperature dependences of the depolariza-

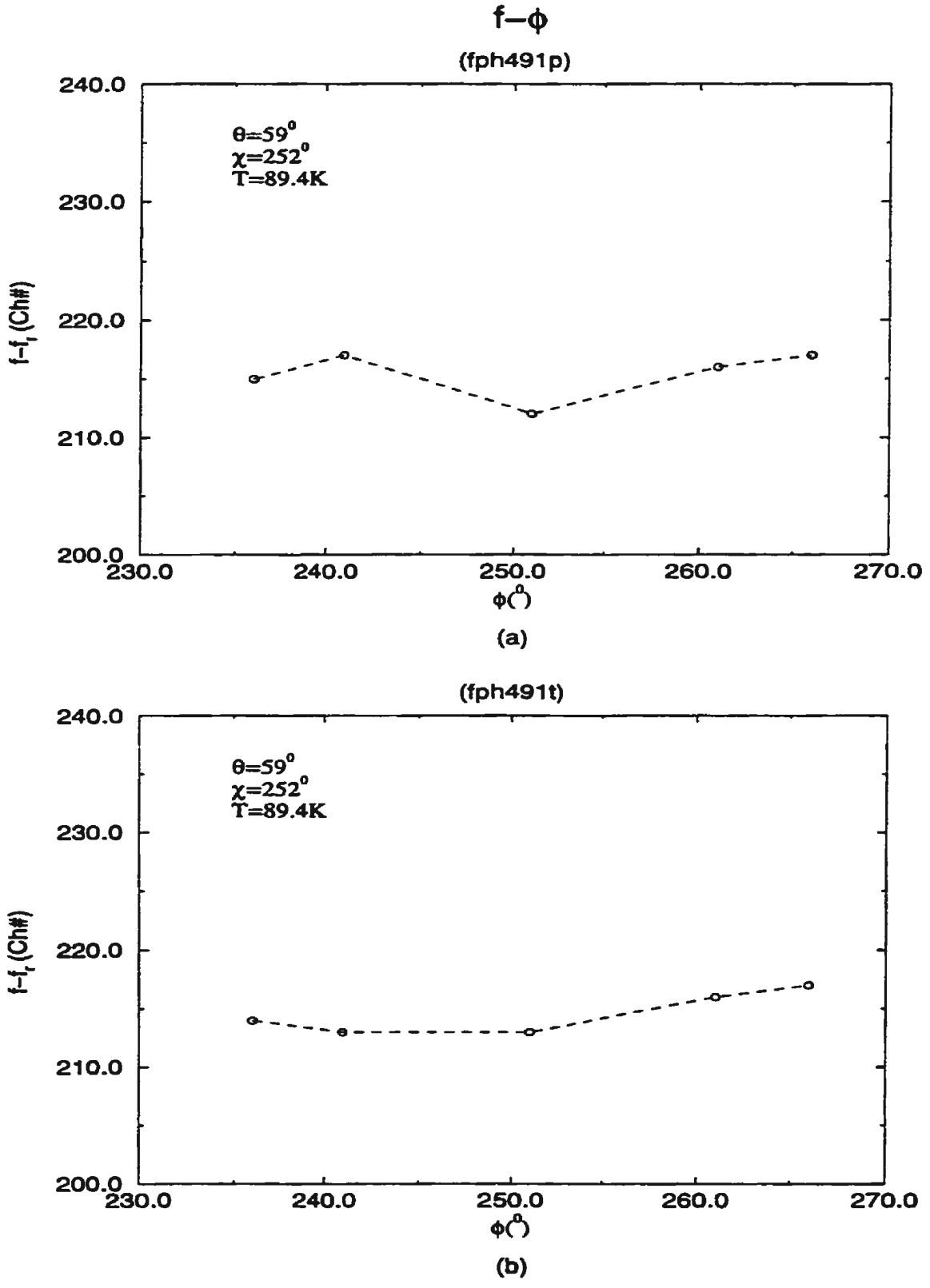

Figure 5.14: f-ϕ Relation of Crystal #49. (a) Parallel (b) Perpendicular

tion ratios of Figure 5.3, 5.5 and 5.6, we can find that the two kinds of temperature dependence are correlated, for example, the maximum of ρ corresponding to the maximum of width in the depolarized (parallel) component.

The width is connected to the damping (anharmonic terms) [33, 44]. When the temperature changes, the damping (the coupling between different modes) also changes. When the temperature is close to 20.6 K, the phase transition will begin (orientation change), this might have some contribution to the width at low temperature.

For the same temperature, the widths change with orientation, and this is shown in Figure 5.18.

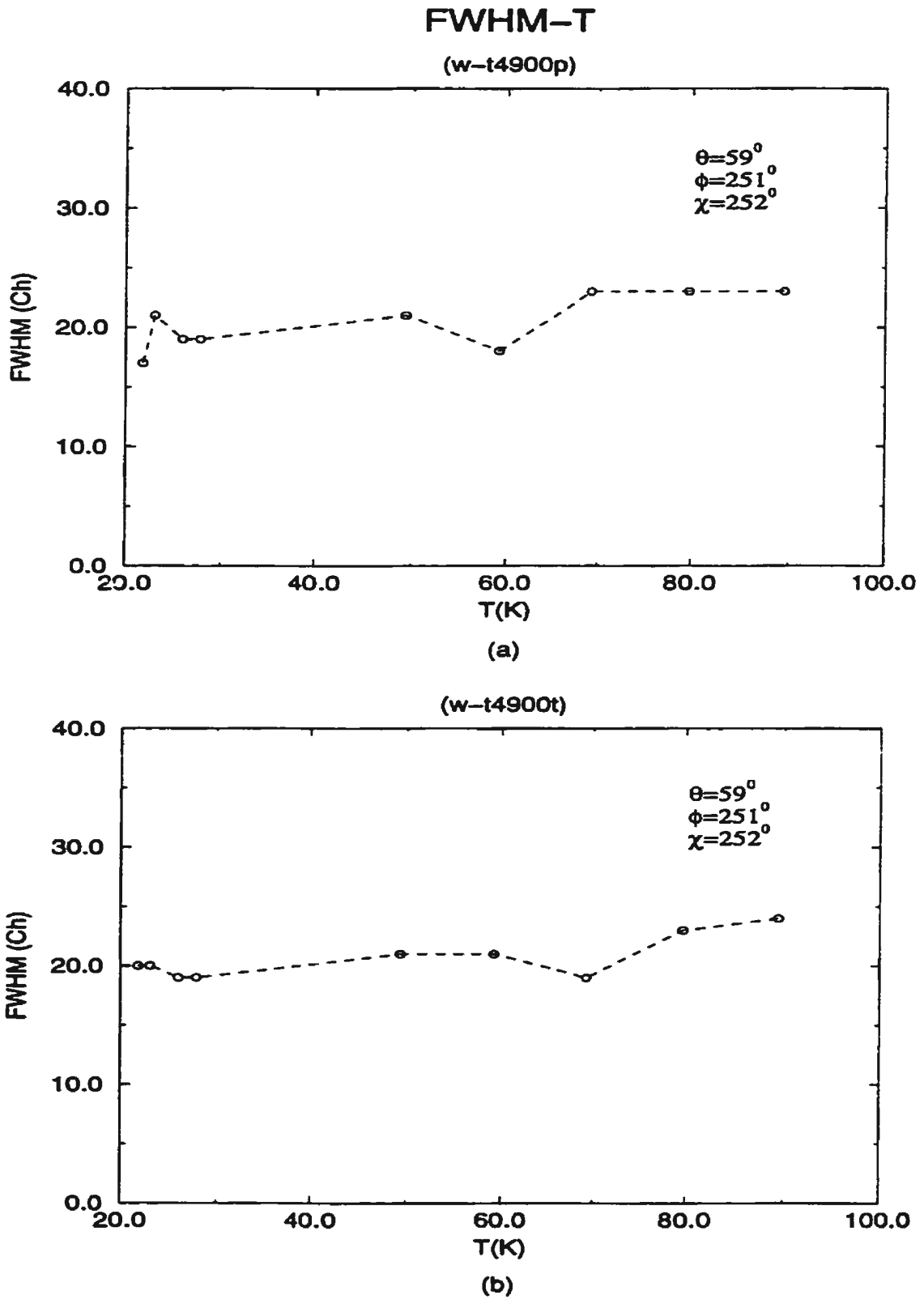

Figure 5.15: Width-T Relation of Crystal #49. (a) Parallel (b) Perpendicular

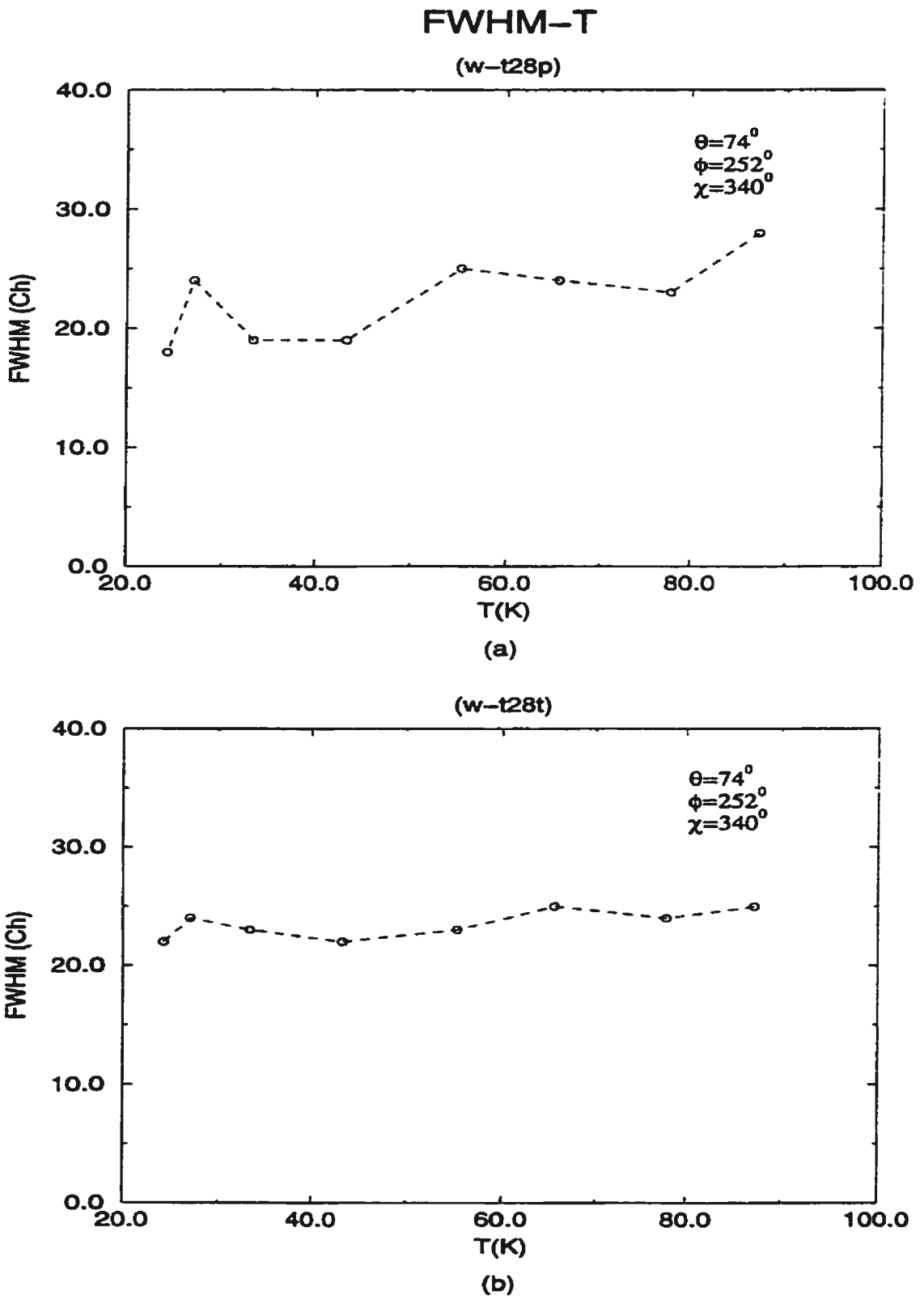

Figure 5.16: Width-T Relation of Crystal #28. (a) Parallel (b) Perpendicular

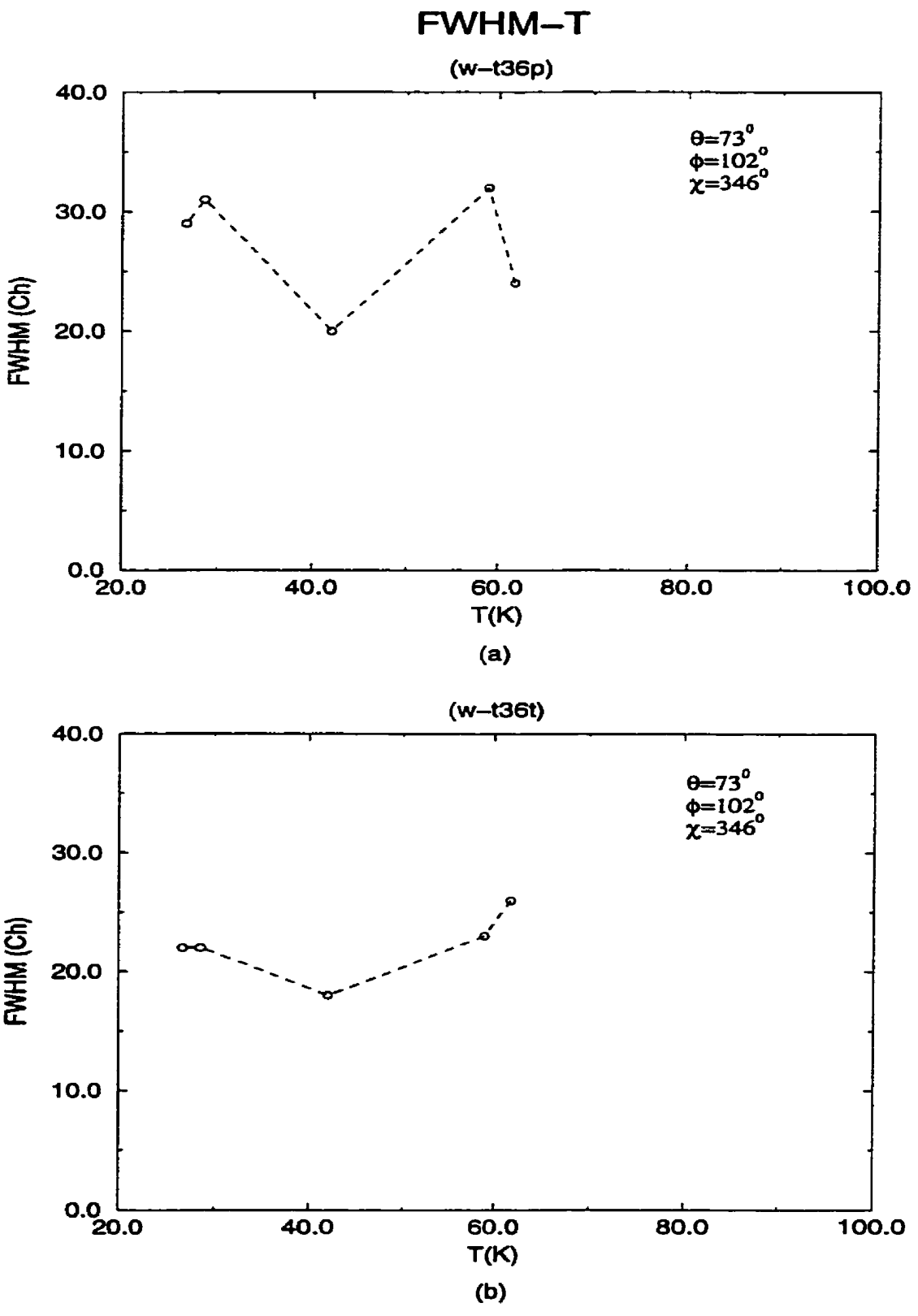

Figure 5.17: Width-T Relation of Crystal #36. (a) Parallel (b) Perpendicular

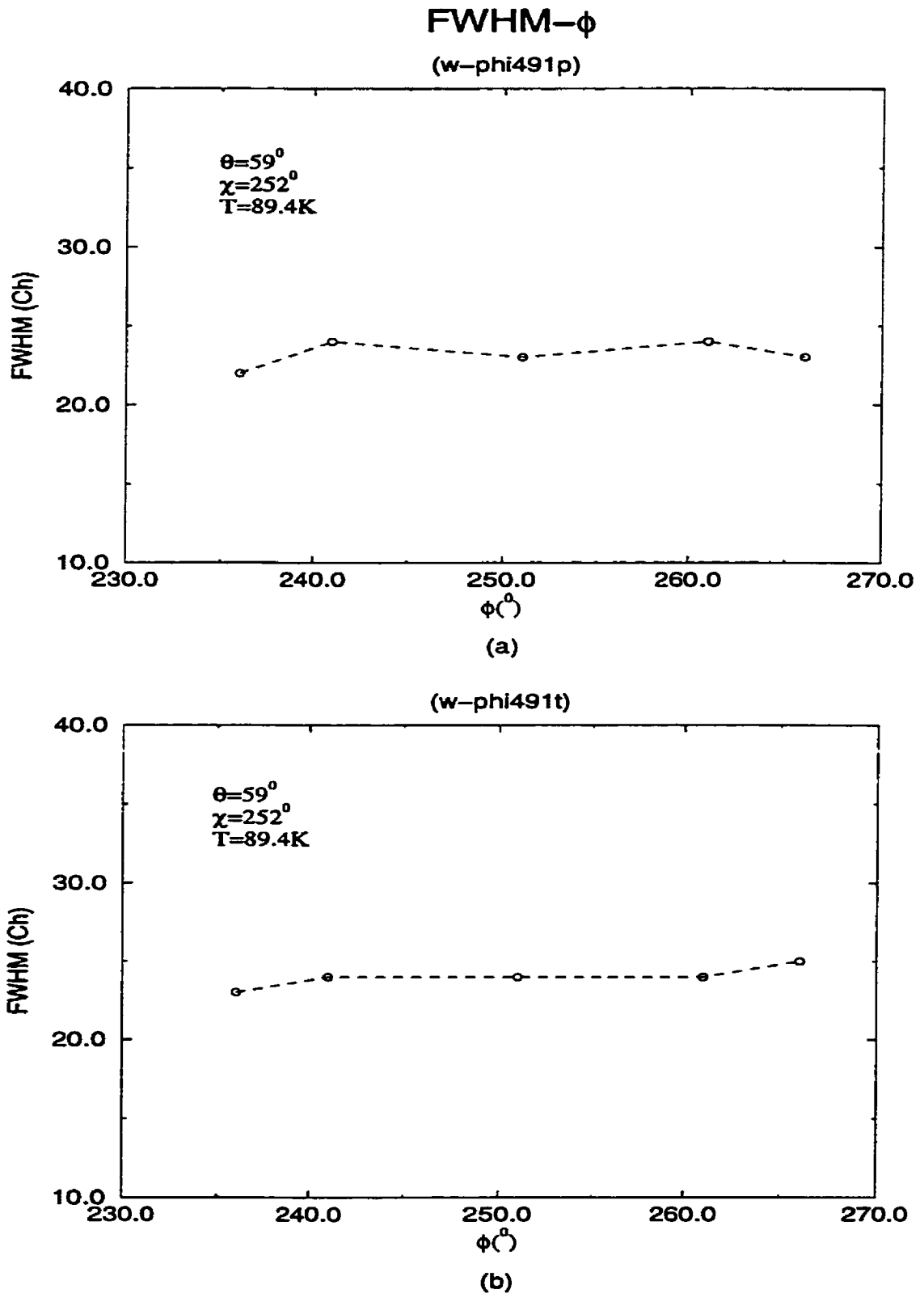

Figure 5.18: Width-ϕ Relation of Crystal #49. (a) Parallel (b) Perpendicular

5.4 Lineshape Fitting and Conclusion

We did the fitting for the laser line by using the Airy function [37],

$$y = \frac{A_0}{[1 + A_1 sin^2(\frac{\pi(x-x_0)}{248})]}, \tag{5.3}$$

where y is the intensity, x is the channel number, x_0 is the centre of the spectrum, A_0 and A_1 are fitting parameters.

The result of the fitting is shown in Figure 5.19 by the solid line. The fitting parameters are $A_0 = 2.286 \times 10^6$, $A_1 = 523.0$. From A_1, we obtain the FWHM of laser $\Gamma_{laser} = 7ch$.

Then, we used the program to do the deconvolution based on equations 3.28 to 3.31. The results are shown in Figure 5.20, where circles are experimental results of the observed spectrum of crystal #36 at 42.0 K, the solid line is the result of fitting before deconvolution, the dashed line was the result of deconvolution.

In the beginning, we used the following function to do the fitting for the observed spectrum (before deconvolution)

$$y = \frac{L_0(1 + A_1 x + A_2 x^2 + A_3 x^3)}{[1 + L_1(x - x_0)^2]} \tag{5.4}$$

We found that the A_1, A_2 and A_3 were very small. This indicated that observed spectrum is of Lorentzian shape. Therefore we used the Lorentzian function to do the fitting for the observed spectrum. The Lorentzian function is

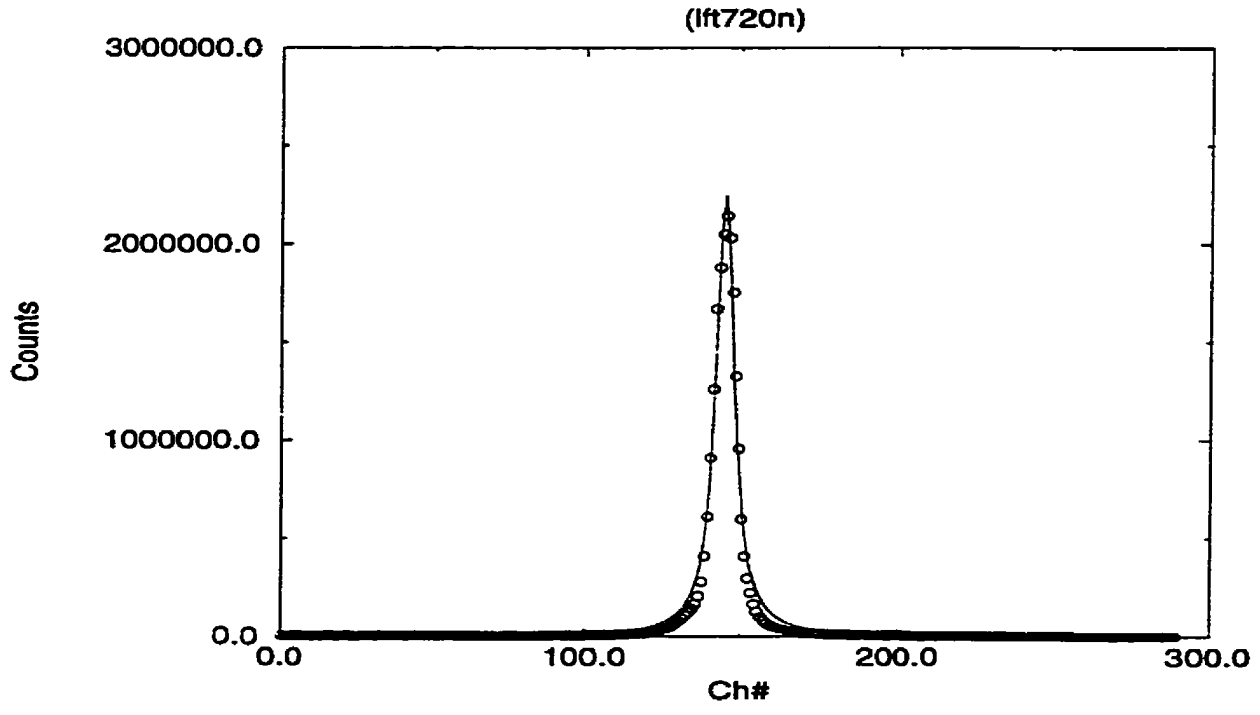

Figure 5.19: The Fitting of The Laser Line

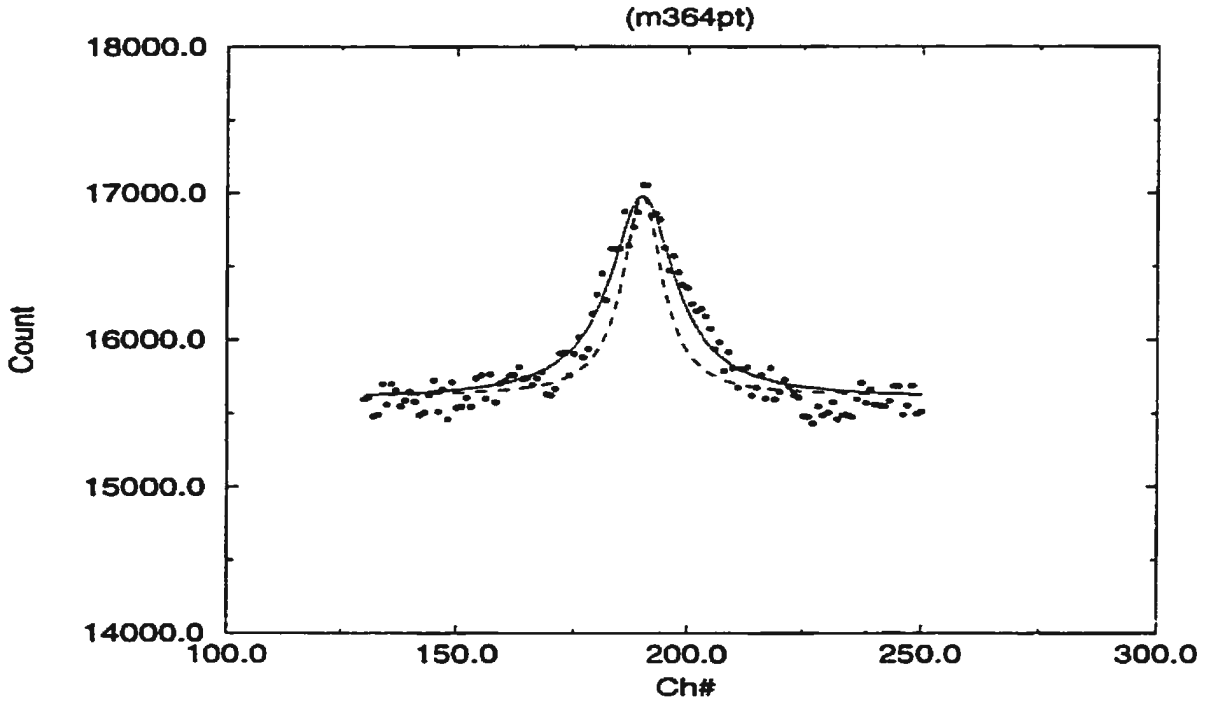

Figure 5.20: Deconvolution of Raman Line

$$y = \frac{L_0}{[1 + L_1(x - x_0)^2]} \tag{5.5}$$

Figure 5.21 shows the Lorentzian fitting of the deconvoluted Raman line. From the fitting parameters, we obtain $\Gamma = 11$ *ch*.

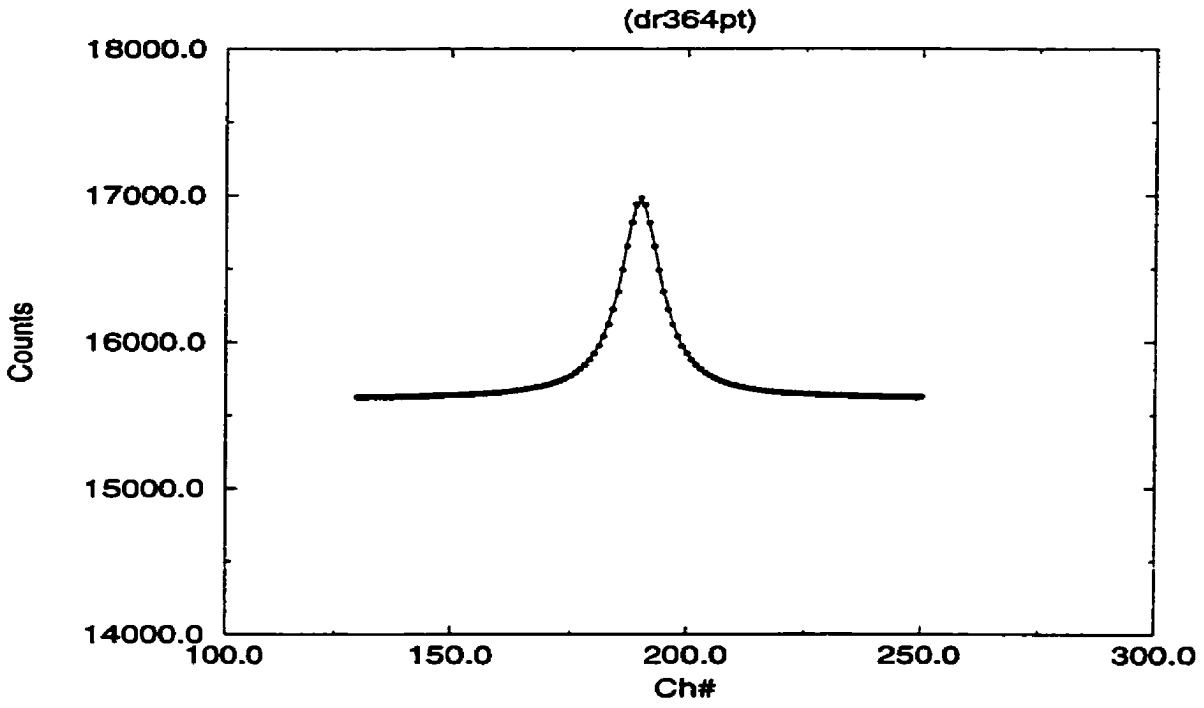

Figure 5.21: Fitting of The Deconvoluted Raman Line

In conclusion, we measured the Raman spectra of ν_1 for crystal CH_4, and found that the frequency, width and the depolarization ratio of the spectra changed with the temperature and the orientation of the crystals.

These changes depend to the following factors: (1)changes in volume ; (2) Vibration-rotation (Coriolis type) interactions; (3) probably molecular orientation change in some temperature range.

We also did the lineshape fitting and deconvolution, the results indicate that the Raman spectra were basically Lorentzian shape.

Further experimental and theoretical investigations are needed to fully understand the causes for the depolarization ratios.

The equipment and the method developed in this work can be used to measure and analyse other modes of methane and other molecular crystals.

Bibliography

[1] M. S. Costantino and W. B. Dsnirld, J. Chem. Phys. 62, 764 (1975).

[2] T. S. Culler and D. Schiferl, J. Phys. Chem. 97, 703 (1993).

[3] Z. Clusius, Phys. Chem. 3, 41 (1929).

[4] O. N. Trapeznikowa, and G. A. Miljution, Nature 144, 632 (1939).

[5] A. Shallamach, Proc. Roy. Soc. (London) A171, 569 (1939).

[6] D. Fabre, M. M. Théry, H. Vu, and K. Kobashi, J. Chem. Phys. 71, 3081 (1979).

[7] R. Stevenson, J. Chem. Phys. 27, 656 (1957).

[8] A. J. Nijman and N. J. Trappeniers, Chem. Phys. 47, 188 (1977).

[9] H.M. James and T. A. Keenan, J. Chem. Phys. 31, 12 (1959).

[10] B. W. Baran, Chem. Phys. Letter 176, 509 (1991).

[11] T. Yamamoto, Y. Kataoka, and K. Okada, J. Chem. Phys. 66, 2701 (1977).

[12] D. Fabre and M. M. Thiéry, J. Chem. Phys. 76, 4817 (1982).

[13] S. K. Sharma, H. K. Mao, and P. M. Bell, Year Book (Carnegie Institution) 351 (1979).

[14] M. J. Clouter, H. Kiefte and R. K. Jain, J. Chem. Phys. 73, 673 (1980).

[15] E. B. Wilson Jr., J. C. Decius and P. C. Cross, Molecular Vibrations (1955).

[16] G. Herzberg, Molecular Spectra and Molecular Structure (1954).

[17] F. A. Cotton, Chemical Applications of Group Theory (1971).

[18] R. G. Dickinson, R. T. Dillon and F. Rasetti. Phys. Rev. 34, 582 (1929).

[19] D. M. Dennison, Astrophys. J. 62, 84 (1925).

[20] H. H. Nielsen, Phys. Rev. 48, 864 (1935).

[21] S. Bhagavantam, Nature, 129, 830 (1932)

[22] G. E. MacWood and H. C. Urey, J. Chem. Phys. 4, 402 (1936)

[23] M. J. Clouter, Ann. Rev. Phys. Chem. 39, 69 (1988).

[24] J. H. Colwell, E. K. Gill, and J. A. Morrison, J. chem. Phys. 36, 2223 (1962).

[25] J. H. Colwell, E. K. Gill, and J. A. Morrison, J. chem. Phys. 39, 635 (1963).

[26] W. Press, J. Chem. Phys. 56, 2597 (1972).

[27] A. Cabana and Nguyen Dinh Thé, Can. J. Chem. 55, 3862 (1977).

[28] M. M. Thiery, D. Fahre and K. Kobashi, J. Chem. Phys. 83, 6165 (1985)

[29] A. Anderson and R. Savoie, J. Chem. Phys. 43, 3468 (1965).

[30] A. Shallamach, Proc. Roy. Soc. (London) A 171, 569 (1939).

[31] T. C. Damen, S. P. S. Porto, and B. Tell, Phys. Rev., 142, 570 (1966).

[32] J. C. Decius and R. M. Hexter, Molecular Vibrations in Crystals (1977).

[33] P. M. A. Sherwood, Vibrational Spectroscopy of Solids (1972).

[34] S. Califano, Vibrational Spectroscopy of Molecular Liquids and Solids (1980).

[35] R. G. Snyder, J. Molec. Spectrosc. 37, 353 (1971).

[36] J. Zhao and R. L. McCreery, Langmuir, 11, 4036 (1995).

[37] M. J. Clouter, H. Kiefte, and C. G. Deacon, Phys. Rev. A 33, 2749 (1986).

[38] K. M. Liang, Mathematical Method in Physics (1979).

[39] S. F. Ahmad, Ph.D. Thesis, Memorial Univerity of Newfoundland, St. John's, Newfoundland (1980).

[40] V. Askarpour, Ph.D. Thesis, Memorial Univerity of Newfoundland, St. John's, Newfoundland (1991).

[41] G. G. Mu and Y. L. Zhang, Optics (1978).

[42] E. J. Rose, E. Whitewolf, and F. G. Baglin, J. Chem. Phys. 97, 4596 (1992).

[43] J-E. Lolck and A. Robiette, J.Mol. Spetrosc. 88, 14 (1981).

[44] A. Anderson, The Raman Effect (1971).

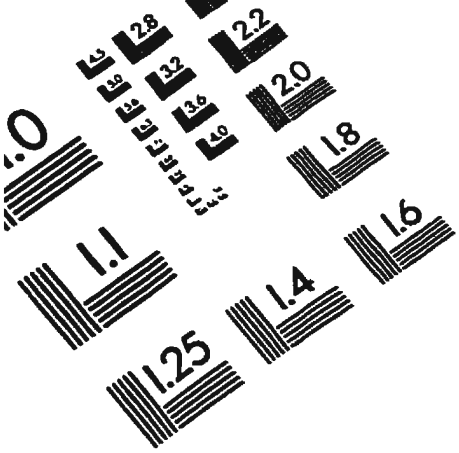

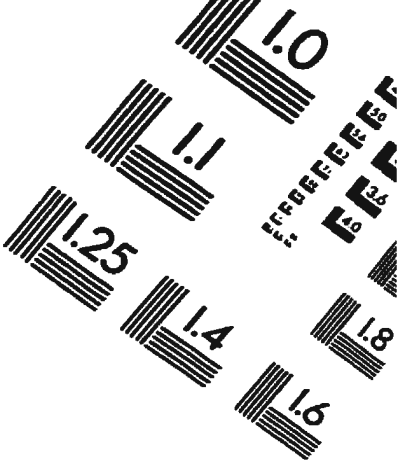

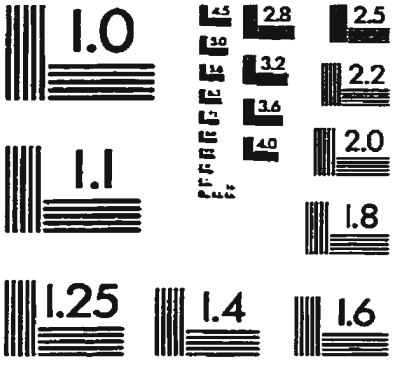

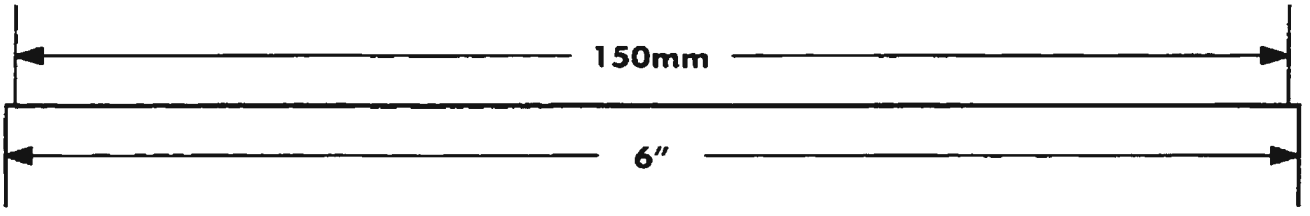

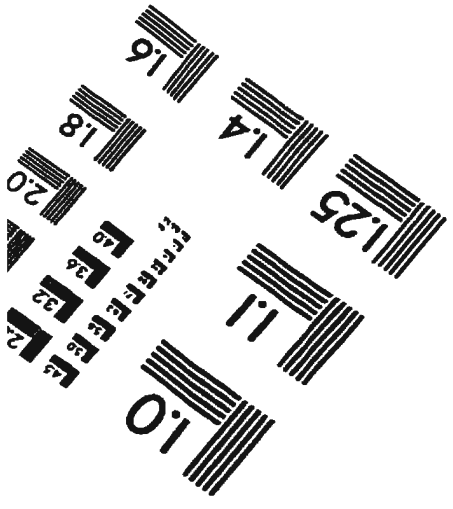

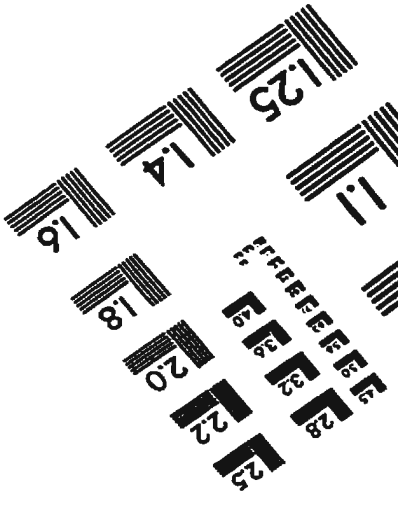

APPLIED IMAGE, Inc
1653 East Main Street
Rochester, NY 14609 USA
Phone: 716/482-0300
Fax: 716/288-5989